



TOI-2046b, TOI-1181b, and TOI-1516b, three new hot Jupiters from TESS: planets orbiting a young star, a subgiant, and a normal star

Downloaded from: <https://research.chalmers.se>, 2024-04-19 15:03 UTC

Citation for the original published paper (version of record):

Kabath, P., Chaturvedi, P., MacQueen, P. et al (2022). TOI-2046b, TOI-1181b, and TOI-1516b, three new hot Jupiters from TESS: planets orbiting a young star, a subgiant, and a normal star. *Monthly Notices of the Royal Astronomical Society*, 513(4): 5955-5972. <http://dx.doi.org/10.1093/mnras/stac1254>

N.B. When citing this work, cite the original published paper.

TOI-2046b, TOI-1181b, and TOI-1516b, three new hot Jupiters from *TESS*: planets orbiting a young star, a subgiant, and a normal star

Petr Kabáth^{1,★}, Priyanka Chaturvedi,² Phillip J. MacQueen,³ Marek Skarka¹, Ján Šubjak,^{1,4} Massimiliano Esposito,² William D. Cochran,⁵ Salvatore E. Bellomo,⁶ Raine Karjalainen¹, Eike W. Guenther,² Michael Endl,⁷ Szilárd Csizmadia⁸, Marie Karjalainen,¹ Artie Hatzes,² Jiří Žák,⁹ Davide Gandolfi⁶, Henri M.J. Boffin⁹, Jose I. Vines¹⁰, John H. Livingston¹¹, Rafael A. García,¹² Savita Mathur,^{13,14} Lucía González-Cuesta,^{13,14} Martin Blažek^{1,15}, Douglas A. Caldwell,¹⁶ Knicole D. Colón,¹⁷ Hans Deeg^{13,14}, Anders Erikson,⁸ Vincent Van Eylen¹⁸, William Fong,¹⁹ Malcolm Fridlund,^{20,21} Akihiko Fukui^{13,22}, Gábor Fűrész,¹⁹ Robert F. Goeke,²³ Elisa Goffo,^{2,6} Steve Howell,²⁴ Jon M. Jenkins,²⁴ Peter Klagyivik,⁸ Judith Korth,²⁵ David W. Latham,²⁵ Rafael Luque,²⁶ Dan Moldovan,²⁷ Felipe Murgas,¹³ Norio Narita,^{13,22,28,29} Jaume Orell-Miquel,^{13,14} Enric Palle,^{13,14} Hannu Parviainen,^{13,14} Carina M. Persson,²⁰ Phillip A. Reed,³⁰ Seth Redfield³¹, George R. Ricker,²³ Sara Seager,^{19,32,33} Luisa Maria Serrano⁶, Avi Shporer,¹⁹ Alexis M. S. Smith,⁸ Noriharu Watanabe³⁴, Joshua N. Winn³⁵ and the KESPRINT team

Affiliations are listed at the end of the paper

Accepted 2022 April 27. Received 2022 March 20; in original form 2021 September 29

ABSTRACT

We present the confirmation and characterization of three hot Jupiters, TOI-1181b, TOI-1516b, and TOI-2046b, discovered by the *TESS* space mission. The reported hot Jupiters have orbital periods between 1.4 and 2.05 d. The masses of the three planets are $1.18 \pm 0.14 M_J$, $3.16 \pm 0.12 M_J$, and $2.30 \pm 0.28 M_J$, for TOI-1181b, TOI-1516b, and TOI-2046b, respectively. The stellar host of TOI-1181b is a F9IV star, whereas TOI-1516b and TOI-2046b orbit F main sequence host stars. The ages of the first two systems are in the range of 2–5 Gyrs. However, TOI-2046 is among the few youngest known planetary systems hosting a hot Jupiter, with an age estimate of 100–400 Myrs. The main instruments used for the radial velocity follow-up of these three planets are located at Ondřejov, Tautenburg, and McDonald Observatory, and all three are mounted on 2–3 m aperture telescopes, demonstrating that mid-aperture telescope networks can play a substantial role in the follow-up of gas giants discovered by *TESS* and in the future by *PLATO*.

Key words: techniques: radial velocities – techniques: spectroscopic – planets and satellites: detection – stars: individual: TOI-1181, TOI-1516, TOI-2046.

1 INTRODUCTION

Hot Jupiters are planets with a mass and radius similar to Jupiter while orbiting their host star in less than about 10 d. Due to their short proximity to their stellar host, hot Jupiters belong to an extremely puzzling group of planets from the evolutionary point of view. Already the first hot Jupiter ever discovered, 51 Peg b, raised the question of the formation and evolution of such systems (Mayor & Queloz 1995). Immediately, some classical theories of gas planet formation were challenged (Pollack et al. 1996).

In spite of over 25 yr of studies of hot Jupiters, there are at least two very good reasons to continue such work:

- 1) insights into planet formation
- 2) atmospheric characterization

Although hot Jupiters were the first exoplanets to be discovered, this is an observational bias due to their short orbital periods and large sizes. Exoplanet surveys later showed that the occurrence rate of hot Jupiters is about 0.43 per cent (Masuda & Winn 2017) – less than the 5.2 per cent fraction of Jupiter-sized planets on longer orbits and significantly lower than the occurrence rates of smaller planets (Fressin et al. 2013). However, the occurrence rate of giant planets differs also based on the metallicity of the host star, with metal-rich stars being more likely to host a giant planet (Wang et al. 2015).

It is still not clear whether hot Jupiters formed *in situ* (Batygin, Bodenheimer & Laughlin 2016) or if they formed far away from their host star and migrated inwards (Heller 2019). Furthermore, systems with several Jupiter-sized planets such as HR 8799 are most likely very rare (Marois et al. 2008; Wright et al. 2009). This particular system, HR 8799, is also an example of a young exoplanetary system of an age of a few hundreds of millions of years (Song et al. 2001). Only a handful of such young systems are known. The youngest fully

* E-mail: petr.kabath@asu.cas.cz

characterized gas giant in terms of mass and radius is the recently discovered *TESS* planet, HIP 67522 b, of about one Jupiter mass with an age of 17 ± 2 Myrs (Rizzuto et al. 2020). Young hot Jupiters are important objects for understanding the evolution of exoplanetary systems as well as the formation history of systems with smaller planets (Weiss et al. 2017; Huang et al. 2020c).

Hot Jupiters are also interesting targets for investigating exo-atmospheres, as the atmospheric signatures of large gas planets can be detected even with mid-sized aperture telescopes from the ground (Wytttenbach et al. 2015; Žák et al. 2019). In some cases, the atmospheres of hot Jupiters might be extended and extremely hot (Cauley et al. 2021; Yan et al. 2021). Nevertheless, atmospheric processes in hot Jupiters are now being understood at a rapid pace and new models are calculated to understand the composition of atmospheres of giant planets (Gao et al. 2020).

Finally, one should also mention here the aspect of telescope time optimization during the ground-based follow-up of exoplanetary candidates. Hot Jupiters are indeed ideal targets for mid-aperture telescopes equipped with precise spectrographs. Such instruments are capable of performing the necessary confirmation and in some cases, even allow their characterization. Mid-aperture class telescopes are ideal instruments to exclude false positives for transit detections. The typical global rate of false positives in the *Kepler* sample is about 6–7 per cent, up to 17 per cent for giant planets only (Fressin et al. 2013). The *TESS* mission global false positives rate is about 25 per cent (Guerrero et al. 2021). Therefore, the confirmation of transit candidates requires many hours of telescope time.

In this paper, we report the confirmation of the *TESS* discovery of three gas giant planets on short orbits. Planetary candidates TOI-1516b, TOI-1181b, and TOI-2046b were confirmed via a coordinated radial-velocity (RV) follow-up monitoring at the Ondřejov 2-m *Perek* telescope (Kabáth et al. 2020), at the *Alfred Jensch* 2-m telescope in Tautenburg (Hatzes, Guenther & Kürster 2003), and at the 2.7-m telescope at McDonald Observatory (Tull et al. 1995), as part of a joint KESPRINT effort.

The KESPRINT¹ consortium has been a major contributor for the characterization of gas planets (Grziwa et al. 2016; Johnson et al. 2016, 2018; Eigmüller et al. 2017; Smith et al. 2017, 2019; Barragán et al. 2018; Hjorth et al. 2019) found by the *K2* mission (Howell et al. 2014), and currently also for small planets (Gandolfi et al. 2019; Esposito et al. 2019; Bluhm et al. 2020; Carleo et al. 2020; Fridlund et al. 2020; Luque et al. 2021; Van Eylen et al. 2021) found by the *TESS* mission (Ricker et al. 2015). Besides small planets, KESPRINT also led the characterization of the first transiting brown dwarf found by *TESS*, TOI-503b (Šubjak et al. 2020).

2 OBSERVATIONAL DATA SETS

Here, and in the following section, we describe the data flow process from the *TESS* discovery light curves up to the RV follow-up observations.

2.1 *TESS* light curves

TESS is a mission designed to detect exoplanets from space, using the transit method (Ricker et al. 2014). The spacecraft consists of four identical cameras with four 2000×2000 CCDs monitoring a field-of-view of $24^\circ \times 24^\circ$. The mission covers about 85 per cent of the sky. Until July 2020, *TESS* recorded every 2 min the flux of over

200 000 main-sequence stars. *TESS* also obtained full-frame images (FFIs) of the entire, four camera field-of-view at a cadence of 30 min. The hot Jupiters reported in this article were observed during the Northern hemisphere monitoring campaign in 2019 and 2020. All three systems were identified by the *TESS* Quick Look Pipeline (QLP; Huang et al. 2020a, b).

TESS observed TOI-1181 in sectors 14, 15, 17, 18, 19, 20, 21, 22, 23, 24, 25 and 26, and 40 and an alert was issued by the *TESS* Science Office on 2019 August 27 (Guerrero et al. 2021). The resulting Data Validation reports (Twicken et al. 2018; Li et al. 2019) are exceptionally clean and the difference image centroiding locates the source of the transit signatures to within 2.5 arcsec. There are no nearby stars in the *TESS* Input Catalog (TIC) sufficiently bright to explain the transit signature as a background eclipsing binary.

TOI-1516 was observed in sectors 17, 18, 24, and 25 and an alert was issued on 2019 December 5, while TOI-2046 was observed in sectors 18, 19, 24, and 25 and an alert issued on 2019 June 19. The cutoff images with each target were extracted from the *TESS* Target-Pixel-Files (TPF) with the default optimum aperture using the LIGHTKURVE v 2.0 package (Lightcurve Collaboration 2018). The images are shown in the left-hand panels of Fig. 1. In order to inspect initially the *TESS* light curves of the three systems, we used again LIGHTKURVE 2.0 with the data downloaded from the MAST archive.²

We show the light curves of the three systems obtained with the Simple Aperture Photometry (SAP) pipeline by the Science Processing Operations Center (SPOC; Twicken et al. 2010; Jenkins et al. 2016; Morris et al. 2020) in the right-hand side of Fig. 1. The full analysis with our noise model description is presented in 3.1.

Catalogue parameters describing the three systems including *TESS*, optical, and IR magnitudes and coordinates are summarized in Table 1.

2.2 Ground-based photometric follow-up

In this section, we describe the ground-based photometric follow-up to check for potential contamination and confirm transit on target. All the presented data were used for a joint fit with the *TESS* data and with the spectroscopic data sets.

2.2.1 The Carlson R. Chambliss Astronomical Observatory

The Carlson R. Chambliss Astronomical Observatory (CRCAO) is located on the campus of Kutztown University in Pennsylvania and operates a fork-mounted 0.6-m Ritchey-Chrétien optical telescope with a focal ratio of $f/8$. The imaging CCD (KAF-6303E) camera has an array of $3k \times 2k$ ($9 \mu\text{m}$) pixels and the system covers a field of view of $19.5 \text{ arcmin} \times 13.0 \text{ arcmin}$. The CCD is cooled to -30°C . With 2×2 binning, the pixel scale is 0.76 arcsec, and the telescope is auto-guided with a total drift of less than 10 pixels throughout an entire night of continuous observations. Seeing at CRCAO is typically about 3 arcsec.

CRCAO observed a full transit of TOI-1181 b on UT 2019 September 25, with 311 consecutive 60 s exposures in the R_C band. However, the observing sequence was interrupted due to a technical problem between fractions of BJD 0.7–0.8, as presented at the top of Fig. A1. CRCAO also observed a full transit of TOI-1516 b on 2020 August 10, with 205 consecutive 90 s exposures in the R_C band. Both data sets were detrended with airmass. The light curve is shown at the bottom of Fig. A1.

¹<http://kesprint.science>

²<https://mast.stsci.edu/portal/Mashup/Clients/Mast/Portal.html>

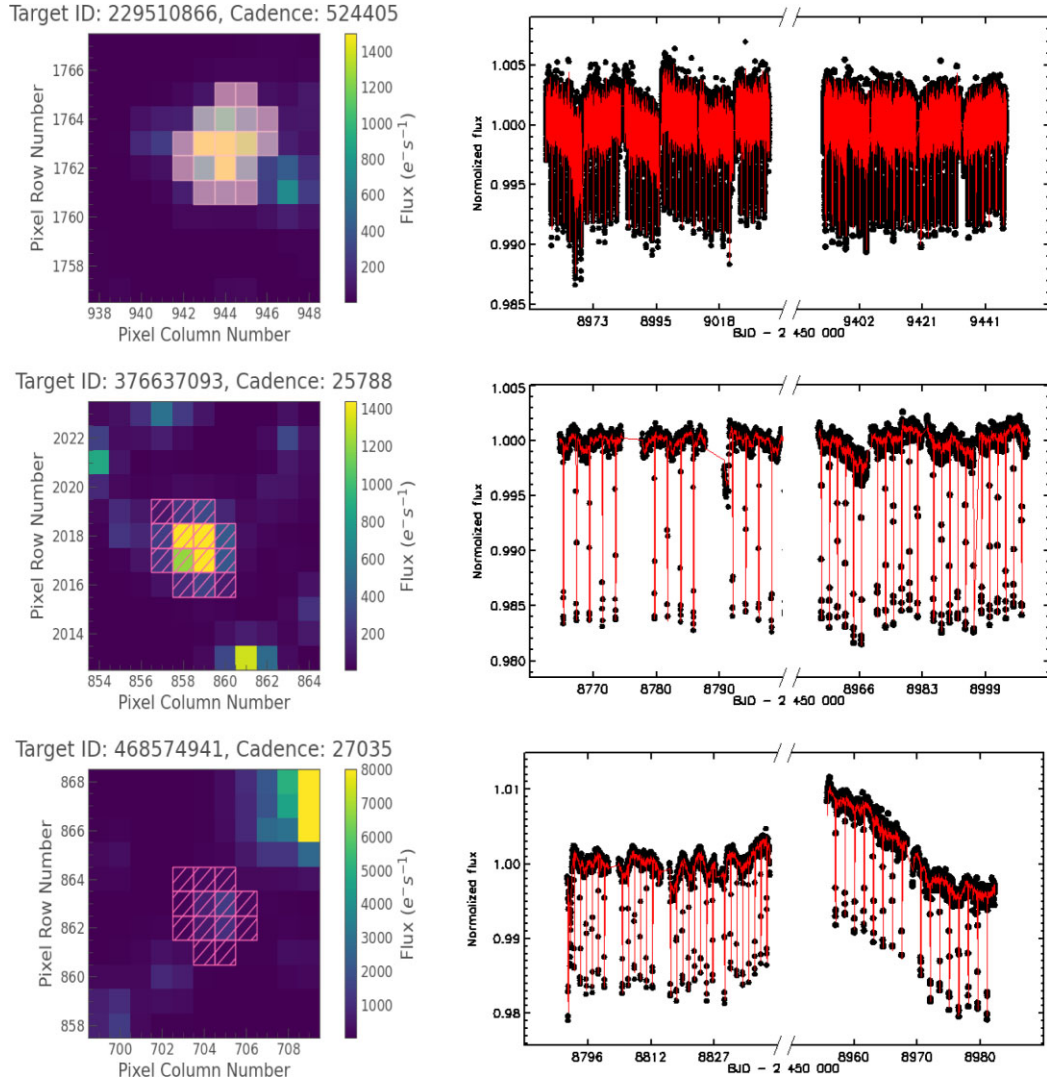


Figure 1. In the left hand panels, the cut-off images from the TPF files are presented with the photometric apertures in pink for stars TOI-1181 (upper panel), TOI-1516 (central panel), and TOI-2046 (bottom panel). The corresponding TESS-SPOC data pipeline processed light curves (SAP, black dots) for the three systems are shown in the right hand panels with the red fitted model obtained with the TRANSIT AND LIGHT CURVE MODELLER (TLCM) code described in Section 3.

Table 1. Observational characteristics of the host stars TOI-1181, TOI-1516, and TOI-2046.

System	TOI-1181	TOI-1516	TOI-2046
TIC number	TIC 229510866	TIC 376637093	TIC 468574941
R.A.	19 ^h 48 ^m 51 ^s .810	22 ^h 40 ^m 20 ^s .261	01 ^h 04 ^m 44 ^s .362
Dec	+64° 21′ 15″.66	+69° 30′ 13″.45	+74° 19′ 52″.85
Gaia parallax (mas)	3.22 ± 0.01	4.0540 ± 0.0098	3.47 ± 0.01
TESS _{mag}	10.079 ± 0.009	10.377 ± 0.006	10.996 ± 0.006
V _{mag}	10.582 ± 0.006	10.858 ± 0.008	11.552 ± 0.018
Gaia _{mag}	10.4776 ± 0.0003	10.7156 ± 0.0002	11.4128 ± 0.0005
J _{mag}	9.55 ± 0.02	9.92 ± 0.03	10.42 ± 0.02
H _{mag}	9.33 ± 0.02	9.70 ± 0.03	10.13 ± 0.03
K _{mag}	9.22 ± 0.02	9.67 ± 0.02	10.09 ± 0.02
WISE _{3.4μm}	9.21 ± 0.02	9.60 ± 0.02	10.08 ± 0.02
WISE _{4.6μm}	9.24 ± 0.02	9.63 ± 0.02	10.10 ± 0.02
WISE _{12μm}	9.24 ± 0.02	9.61 ± 0.03	10.00 ± 0.05
WISE _{22μm}	8.70 ± 0.19	9.41 ± 0.35	8.88 ± N/A

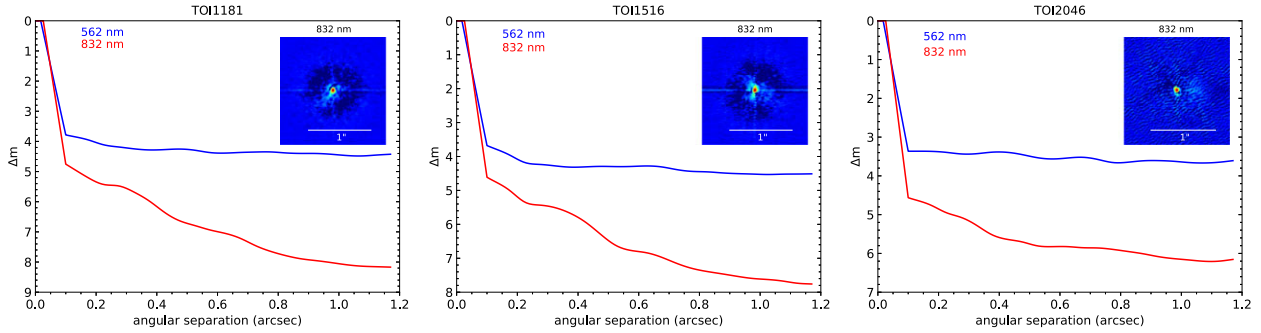


Figure 2. Speckle imaging results of TOI-1181, TOI-1516, and TOI-2046.

2.2.2 MUSCAT2 Observations at the Carlos Sanchez Telescope

The *MUSCAT2* instrument is a four channel imager designed to observe simultaneously in the g , r , i , and z_s photometric bands. It is installed on the 1.52-m *Carlos Sanchez Telescope (TCS)* at the Teide Observatory in the Canary Islands, Spain. Each photometric channel is equipped with one 1024×1024 CCD camera with a field of view of 7.4×7.4 arcmin (Narita et al. 2019). One transit of TOI-1181b was observed with *MUSCAT2* on the night of 2019 November 9, using exposure times of 5, 7, 11, and 7 s for the g , r , i , and k_s bands, simultaneously. The observations were taken slightly defocused and covered the full transit, with a average seeing trough the night of 1 arcsec. The resulting light curve is plotted in Fig. A2. Table A1 presents the estimated posterior values of the parameters obtained from the full *MUSCAT2* light curve.

2.3 High-resolution imaging

Due to the large pixel scale of the *TESS* detectors, it is important to search for nearby contaminating sources that can dilute the transit depth or lead to false positives (e.g. Ciardi et al. 2015). In particular, those sources not detected in seeing-limited photometry or by Gaia require specialized observational techniques like high spatial resolution imaging to be detected.

On the nights of UT 2020 August 4 and 2021 June 29, we observed TOI-1181, TOI-1516, and TOI-2046 with the 'Alopeke speckle imager (Scott 2019), mounted on the 8.1-m *Gemini North* telescope at Mauna Kea. 'Alopeke has a field-of-view of 6.7 arcsec and it simultaneously acquires data in two bands centred at 562 and 832 nm using high-speed electron-multiplying CCDs (EMCCDs). We collected and reduced the data following the procedures described in Howell et al. (2011). The resulting reconstructed images achieved a contrast of $\Delta\text{mag} \sim 4$ at a separation of 0.2 arcsec in the 832-nm band (see Fig. 2). No contaminants were found.

2.4 Spectroscopic follow-up

We performed spectroscopic follow-up using a network of mid-aperture sized telescopes in the Northern hemisphere. These include the OES located in the Czech Republic, the Tautenburg echelle spectrograph (TCES) in Germany, and the Tull Spectrograph at McDonald Observatory in the U.S.A. These provided the bulk of the data for the orbital solutions. All data sets were obtained between 2020 January and 2021 March. The measured radial velocities are presented in Tables A2–A4.

2.4.1 The OES spectrograph

The OES is installed on the 2-m telescope in Ondřejov, Czech Republic and is operated by the Astronomical Institute of the Czech Academy of Sciences. OES is a fiber-fed spectrograph with resolving power of $R = 50\,000$ (at 500 nm) and wavelength range of 380–900 nm. An accuracy of 70 m s^{-1} in radial velocities is typically achieved for a $V = 6$ star. We use a hollow-cathode comparison frame for the wavelength calibration. A standard spectroscopic data reduction with IRAF scripts was performed on all data sets. The instrument related shifts are corrected by telluric lines using the method of Gray & Brown (2006) and radial velocities are obtained by the cross-correlation method using the `fxcor` task in IRAF. A more detailed description is provided in Kabáth et al. (2020). For the present targets and with an exposure time of 3600 s, the typical SNR of the OES spectra range between 20 and 40.

2.4.2 The TCES spectrograph

The Tautenburg Coudé Echelle spectrograph (TCES) is installed on the 2-m Alfred Jensch telescope operated by the Thuringer Landessternwarte Tautenburg, Germany. The instrument achieves a resolving power of $R = 67\,000$ over the wavelength range from 467 to 740 nm. The spectra can be calibrated with an iodine (I_2) cell. The data reduction is performed with the Tautenburg Spectroscopy Pipeline - τ -spline. The pipeline makes use of standard IRAF and PYRAF routines and the Cosmic Ray code by Malte Tewes based on the method by van Dokkum (2001). All steps are detailed in e.g. Sabotta et al. (2019). The TCES can achieve an RV precision of $3\text{--}5 \text{ m s}^{-1}$ on very bright stars with an iodine cell, but typical RV accuracy on fainter targets is about 70 m s^{-1} ; for more details, see Guenther et al. (2009) and Döllinger et al. (2009). RVs were derived by a PYTHON-based software VELOCITY AND INSTRUMENT PROFILE ESTIMATOR (VIPER)³ (Zechmeister, Köhler & Chamarthi 2021), based on the standard procedure described in Butler et al. (1996), Endl, Kürster & Els (2000). Most of the spectra in Tautenburg were obtained with an iodine cell. Typical SNRs of the TCES spectra are in the range 10–20 with 1800 s exposure time.

2.4.3 The Tull spectrograph

The Tull spectrograph is installed at the 2.7-m telescope of the McDonald Observatory operated by the University of Texas, USA. The instrument is a cross-dispersed white pupil echelle spectrograph. A 2048×2048 pixel CCD at the 'F3' focal position, combined with a

³<https://github.com/mzechmeister/viper>

1.2 arcsec wide entrance slit gives a resolving power of about 60 000 over a wavelength range of 375–1020 nm. A temperature stabilized I₂ vapor absorption cell placed in front of the slit provides the velocity metric. All data were reduced and extracted using an IRAF pipeline script. Precise radial velocities down to a few m s⁻¹ were computed using the Austral pipeline (Endl et al. 2000).

2.4.4 The Tillinghast Reflector Echelle Spectrograph spectrograph

We used the Tillinghast Reflector Echelle Spectrograph (TRES) on Mt. Hopkins, Arizona, to crosscheck and compare the stellar parameters with those derived from our data from the Tull, OES, and TCES spectrographs. During 2019, we obtained two spectra for each system of our targets. The spectrograph has a resolving power of $R = 44\,000$ and covers wavelengths from 390 to 910 nm. The relative RVs that we derive from TRES spectra use multiple echelle orders from each spectrum that are cross-correlated with the highest S/N spectrum of the target star. We omit individual orders with poor S/N and manually remove obvious cosmic rays.

3 DATA ANALYSIS AND PARAMETERS DETERMINATION

In this section, we describe the methods used to analyse our data sets to determine the stellar parameters of the host stars such as radii, masses, effective temperatures, and metallicities, as well as their ages. The photometric light curves were also used to investigate stellar rotation.

3.1 Fitting the light curves with TLMC

We used for our analysis the software package TLMC (Csizmadia et al. 2021). This code is able to perform joint radial velocity and light curve fit, modelling the beaming, ellipsoidal, and reflection effect (Faigler & Mazeh 2011; Shporer 2017; Wong et al. 2020). The noise model is based on the wavelet formulation of Carter & Winn (2009), with the regularization that the standard deviation of the residuals must converge to the average uncertainty of the input photometric data points, thereby avoiding overfitting. The approach was widely tested and the results have shown that, at the signal-to-noise ratio level of the present targets, the method is able to recover all the parameters with 1–2 per cent accuracy (Csizmadia et al. 2021). We fit the transit parameters and the noise model simultaneously. Because of the noise-model applied here, we used the SAP-light curves for this kind of analysis and we kept only those data points with a quality flag of 0. The light curve was in the first step corrected for any potential contamination before modeling, using the CROWDSAP keyword of the TESS FITS-files.

The free parameters were: the scaled semi-major axis, the planet-to-star radius ratio, the impact parameter, and the limb darkening combinations of the quadratic limb darkening law as follows:

$$u_+ = u_a + u_b, u_- = u_a - u_b, \quad (1)$$

as well as the epoch, period, flux zero-level shift, wavelet-based noise model σ_w , σ_r , the systematic velocity of the system (V_γ), radial velocity amplitude (K), and the radial velocity offsets between different spectrographs. Because only FFIs with 30 min integration time were available in the case of TOI-1516 and TOI-2046, we applied five subexposures and numerical integration to get more precise modelled flux values (cf. section 2.11 of Csizmadia 2020). We have run a Genetic Algorithm/Harmony Search to optimize the joint light curve and radial velocity fit, with the results refined by

three chains of Simulated Annealing. This yielded a starting point of the MCMC-analysis. We have run four chains for each system with a thinning factor of five. The chain lengths were at least 100 000 but they were automatically extended if they did not converge. The convergence was checked via the Gelman–Rubin statistic as well as via the estimated sample size. For details, see Csizmadia (2020) and references therein.

As a sanity check, we performed an independent joint analysis of the transit light curves and Doppler measurements of TOI-1181, TOI-1516, and TOI-2046 using the code PYANETI (Barragán, Gandolfi & Antoniciello 2019), which infers the system parameters using a Bayesian approach coupled to Markov chain Monte Carlo simulations. We imposed uniform uninformative priors for all the model parameters and added photometric and RV jitter terms to account for noise not included in the nominal uncertainties. We initially fitted for the eccentricity and angle of periastron adopting the parametrization proposed by Anderson et al. (2011) and found that the eccentricities of the three planets are consistent with zero, with the Bayesian information criterion favouring circular models. We thus fixed the eccentricities to zero in our analysis. We found that the mean densities of the three stars – as derived from the modelling of the transit light curves using Kepler’s third law (Winn 2010) – are consistent with the spectroscopic densities. We also found that system parameters agree well within $\sim 1\sigma$ with those derived with TLMC, corroborating our results.

3.2 TOI-1181 b: A hot Jupiter on a 2.1-d orbit around a subgiant star

We combine here *TESS* with the ground-based *CRCAO* and *MUSCAT2* photometric data and 57 spectra from OES, TCES, and Tull spectrographs. The resulting RVs for all instruments used during the follow-up campaign are listed in Table A2. We also used the TRES spectra.

3.2.1 The host star TOI-1181

First, we combined 13 best SNR spectra from Tautenburg’s TCES (i.e. only the spectra obtained without an Iodine cell and with a better SNR than the OES ones), in order to determine the stellar parameters of the host star. We used the ISPEC software for the analysis (Blanco-Cuaresma et al. 2014; Blanco-Cuaresma 2019). Regions between 490 and 560 nm and between 605 and 627 nm were used to derive the effective temperature, T_{eff} , metallicity, $[\text{Fe}/\text{H}]$, surface gravity, $\log g$ and rotational velocity of the star, $v \sin i$. We used the synthesis method from the code SPECTRUM and MARCS atmosphere models (Gustafsson et al. 2008). We also obtained parameters from the Tull spectra with the KEA pipeline (Endl & Cochran 2016), using synthetic spectra from the library compiled by Kurucz (1993). Another independent parameter set was derived from the analysis of the TRES spectra with EXOFASTv2 (Eastman et al. 2019). The resulting values from these three independent analyses can be compared in Table 2. The same procedure applies for the other two systems discussed in this paper. It appears that the TRES and Tull values for $[\text{Fe}/\text{H}]$ and $\log(g)$ differ from the values derived with ISPEC. The ISPEC values were obtained manually by inspection of the spectra, while the TRES and Tull teams use automatized pipelines which might be biased towards main sequence stellar templates, but TOI-1181 is, as described in the following, an evolved star. Therefore, for further modelling, we use the ISPEC-derived parameters for TOI-1181, that is, effective temperature $T_{\text{eff}} = 5990 \pm 95$ K, gravity $\log g = 3.9 \pm 0.15$, and $v \sin i = 10.2 \pm 1.5$ km s⁻¹.

Table 2. System parameters for host stars of hot Jupiters TOI-1181.01, TOI-1516.01, and TOI-2046.01 obtained by tlcm. Stellar mass and radius are derived from isochrone-fitting as described in Csizmadia (2020).

Parameter	Instrument	TOI-1181b	TOI-1516b	TOI-2046b
a/R_*		$4.19^{+0.06}_{-0.08}$	$6.22^{+0.041}_{-0.077}$	$4.75^{+0.18}_{-0.17}$
R_{planet}/R_*		$0.0764^{+0.0004}_{-0.0004}$	$0.1224^{+0.0005}_{-0.0005}$	$0.1213^{+0.0017}_{-0.0021}$
b		$0.19^{+0.08}_{-0.11}$	$0.09^{+0.10}_{-0.07}$	$0.51^{+0.06}_{-0.07}$
u_+		$0.46^{+0.06}_{-0.06}$	$0.10^{+0.08}_{-0.08}$	$0.39^{+0.24}_{-0.16}$
u_-		$0.16^{+0.19}_{-0.19}$	$0.81^{+0.19}_{-0.19}$	$0.30^{+0.59}_{-0.74}$
Epoch (BJD)–2450 000		$8684.4058^{+0.0017}_{-0.0017}$	$8765.3250^{+0.0001}_{-0.0001}$	$7792.2767^{+0.0024}_{-0.0022}$
Period (days)		$2.103195^{+0.000012}_{-0.000011}$	$2.056014^{+0.000002}_{-0.000002}$	$1.4971842^{+0.0000031}_{-0.0000033}$
σ_r (ppm)		34469^{+589}_{-584}	14950^{+252}_{-252}	24024^{+471}_{-469}
σ_w (ppm)		1046^{+3}_{-3}	299^{+4}_{-4}	576^{+14}_{-14}
V_γ (m s ^{−1})		$119.1^{+15.7}_{-15.8}$	$-397.6^{+39.5}_{-40.7}$	$-12.6^{+5.5}_{-5.5}$
K (m s ^{−1})		$165.6^{+11.4}_{-11.4}$	$460.7^{+9.0}_{-9.0}$	$374.7^{+7.8}_{-7.8}$
RV-offsets (m s ^{−1})				
Ondrejov - TCES		$-118.5^{+34.6}_{-34.5}$	$-116.0^{+44.9}_{-43.1}$	
Tull-TCES		$-50477.5^{+17.1}_{-17.2}$	$-48189.7^{+41.3}_{-40.0}$	
TCES - Tull				$537.7^{+49.4}_{-49.4}$
Ondrejov - Tull				$-9479.6^{+43.3}_{-43.2}$
Derived parameters				
Inclination (°)		$87.0^\circ \pm 1.3^\circ$	$90.0^\circ \pm 0.4^\circ$	$83.6^\circ \pm 0.9^\circ$
Transit duration (h)		$4.057^{+0.014}_{-0.013}$	$2.826^{+0.015}_{-0.014}$	$2.410^{+0.032}_{-0.030}$
ρ_* (kg m ^{−3})		312 ± 16	1090 ± 31	890 ± 98
M_*/M_\odot		1.19 ± 0.18	1.14 ± 0.06	1.13 ± 0.19
R_*/R_\odot		1.75 ± 0.09	1.14 ± 0.02	1.21 ± 0.07
M_{planet}/M_J		1.18 ± 0.14	3.16 ± 0.12	2.30 ± 0.28
R_{planet}/R_J		1.30 ± 0.08	1.36 ± 0.03	1.44 ± 0.11
Stellar parameters				
T_{eff} [K]	Tull	6260 ± 100	6420 ± 100	6160 ± 100
T_{eff} [K]	ISPEC OES/TCES	5990 ± 95	6520 ± 90	6250 ± 140
T_{eff} [K]	TRES	6177 ± 50	6170 ± 52	6143 ± 97
$\log g$ [cgs]	Tull	4.31 ± 0.18	4.25 ± 0.18	4.38 ± 0.18
$\log g$ [cgs]	ISPEC OES/TCES	3.9 ± 0.15	4.25 ± 0.15	4.3 ± 0.15
$\log g$ [cgs]	TRES	4.27 ± 0.08	4.18 ± 0.22	4.35 ± 0.08
Fe/H [dex]	Tull	0.30 ± 0.12	-0.14 ± 0.12	0.04 ± 0.12
Fe/H [dex]	ISPEC OES/TCES	0.05 ± 0.1	-0.05 ± 0.1	-0.06 ± 0.15
Fe/H [dex]	TRES	0.44 ± 0.08	-0.05 ± 0.1	0.29 ± 0.08
v_{ini} [km s ^{−1}]	Tull	10.77 ± 0.30	11 ± 0.4	8.15 ± 0.15
v_{ini} [km s ^{−1}]	ISPEC OES/TCES	10.2 ± 1.5	11.8 ± 1.5	9.8 ± 1.6
v_{ini} [km s ^{−1}]	TRES	11.8 ± 2.0	13.8 ± 2.0	8.8 ± 2.0
Derived stellar parameters	(ARIADNE)			
Stellar radius - R_* (R_\odot)		$1.90^{+0.06}_{-0.10}$	$1.245^{+0.031}_{-0.032}$	$1.237^{+0.036}_{-0.032}$
Stellar mass - M_* (M_\odot)		$1.380^{+0.086}_{-0.082}$	$1.085^{+0.061}_{-0.066}$	$1.153^{+0.10}_{-0.093}$
Age of the host star (Gyr)		$2.59^{+0.43}_{-0.51}$	$4.82^{+2.44}_{-1.29}$	$0.45^{+0.43}_{-0.021}$
Spectral type		F9IV	F8V	F8V

3.2.2 Stellar parameters

We used the ARIADNE⁴ code (Vines & Jenkins 2021) to determine the SED and the mass of the star by fitting the available measurements from various catalogues with various models, described below. The fitted SED of TOI-1181 is shown in the top panel of Fig. 3. ARIADNE

uses as input value the parallax from Gaia EDR3 (Gaia Collaboration 2018, 2016) and models are obtained by convolution with Phoenix v2 (Husser et al. 2013), BT-Cond (Allard, Homeier & Freytag 2012), BT-NextGen (Hauschildt, Allard & Baron 1999; Allard et al. 2012), Castelli & Kurucz (Castelli & Kurucz 2006) and Kurucz (Kurucz 1993) models with the available photometric data in the following bandpasses: UBVRI; 2MASS JHKs; SDSS ugriz; ALL-WISE W1 and W2; Gaia G, RP, and BP; Pan-STARRS griwyz; Stromgren uvby; GALEX NUV and FUV; Spitzer/IRAC 3.6 and 4.5 μm ; TESS;

⁴<https://github.com/jvines/astroARIADNE>

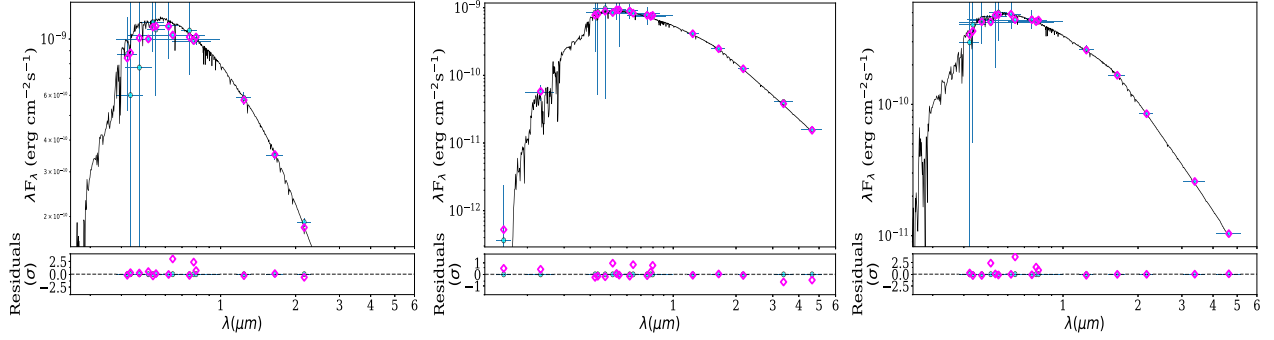


Figure 3. The spectral energy distribution function (SED) fitted by ARIADNE for TOI-1181 (top), TOI-1516 (centre), TOI-2046 (bottom).

Kepler; and NGTS. We also interpolated values for T_{eff} , $\log g$, and $[\text{Fe}/\text{H}]$. The stellar mass M_* was determined from MESA Isochrones and Stellar Tracks models (Dotter 2016). The corresponding derived parameters are reported in Table 2. We used as priors the values of T_{eff} , $[\text{Fe}/\text{H}]$, and $\log g$ determined from the spectra with ISPEC. ARIADNE derived for TOI-1181 a stellar mass of $M_* = 1.38^{+0.086}_{-0.082} M_\odot$, a radius of $R_* = 1.9^{+0.06}_{-0.10} R_\odot$, and an age of $2.59^{+0.43}_{-0.51}$ Gyr.

We further derived the spectral type and luminosity class of TOI-1181 following the method outlined in Frasca et al. (2003) and Gandolfi et al. (2008). Briefly, we fitted the iodine-free Tull spectra of the three stars using the Indo-US grid of stellar templates from Valdes et al. (2004). Prior to the fitting procedure, the resolution of the Tull spectra was degraded to match that of the templates ($R = 5500$) by convolving the Tull spectra with a Gaussian function mimicking the difference between the two instrument profiles. The radial velocity shift between the Tull spectra and Indo-US templates was measured using the cross-correlation technique. We fitted the 4500–6800 Å spectral range, masking out the regions containing telluric lines. We found that TOI-1181 is a somewhat evolved F9 IV star. Further discussion on TOI-1181 is provided in Section 4.

3.2.3 Stellar rotation

To investigate the light variations out of eclipse and their possible connection with stellar variability, we used the PDCSAP data with 1800 s cadence.⁵ After we removed the transits from the light curves, we performed a discrete Fourier transform on the full data sets by using the PERIOD04 software (Lenz & Breger 2005) to get the periodograms (Fig. 4). The frequency spectra of all the three studied stars show peaks above the significance limit defined by $\text{SNR} > 4$ (Breger et al. 1993). To test the nature and stability of the identified peaks, we divided the data sets into segments spanning 20–30 d and performed the frequency analysis on these shorter data sets.

In TOI-1181, we identified three significant peaks at 0.449, 0.264, and 0.114 c/d (periods of 2.22, 3.78, and 8.74 d – top panel of Fig. 4). The peak corresponding to the period of 8.74 d perfectly matches the rotational period calculated from $v \sin i$ (assuming $i = 87^\circ$) and stellar radius ($R_* = 1.75 R_\odot$), $P_{\text{rot}} = 8.7 \pm 1.4$ d (the dash-dotted line in the top panel of Fig. 4). We detected this frequency and its harmonics also in all the subsets therefore making unlikely the instrumental origin of this frequency peak. It is highly likely that these peaks are real and attributed to the rotational period of the

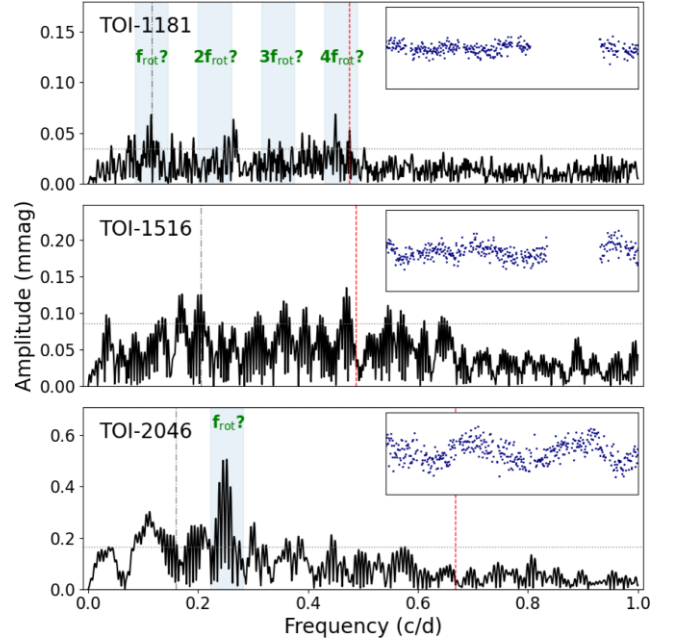


Figure 4. The frequency spectra of the residual light curves (without transits) for the investigated stars. The red dashed vertical line shows the position of the orbital frequency, the grey dash-dotted line shows the position of the expected rotational period calculated from $v \sin i$ and the stellar radius, while the grey dotted lines show the reliability signal-to-noise ratio ($\text{SNR} = 4$) level for the highest peak. The insets show the 10-d segments of the light curves. The vertical range of the insets is 6 mmag.

star. The differential rotation and spots at different latitudes are most likely responsible for the slight difference of the frequency peaks of the harmonics.

3.2.4 Stellar pulsations

We also performed a seismic analysis to look for solar-like oscillations using the TESS light curves. To do so we used two types of light curves: the PDCSAP light curves and light curves obtained with a customized aperture larger than the previous one and that is optimized for asteroseismology. For that second data set, we selected pixels in the target pixel files where the average flux is above $100 \text{ e}^- \text{ s}^{-1}$ and making sure that we do not pick pixels contaminated by a nearby star. For both light curves we removed the planetary transits, outliers, and filled the gaps following García et al. (2011, 2014). Using global seismic scaling relations (Brown 1991; Kjeldsen & Bedding 1995)

⁵Downloaded using LIGHTKURVE v 2.0 package (Lightkurve Collaboration 2018) because the SAP data suffer from strong instrumental effects (see the right-hand panels of Fig. 1).

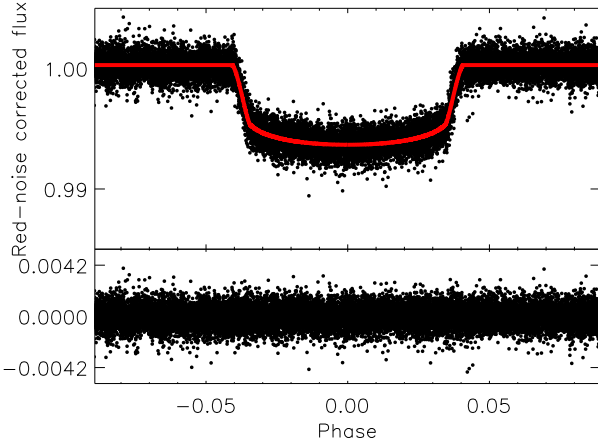


Figure 5. Upper panel: The red-noise corrected *TESS* SAP-fluxes (black dots = observations - red noise component) of TOI-1181 as a function of phase. The model fit is shown with red solid lines. Results obtained by TLMC (see Section 3.1). Lower panel: The residuals of the model fit after subtracting the red noise component from the observations.

where we combined the effective temperature and the surface gravity, we estimated the predicted frequency of maximum power, ν_{\max} , to be around 1000 μHz . From the visual inspection of the power spectrum density computed for both light curves, no obvious acoustic-mode bump is visible around that value. We ran the A2Z pipeline (Mathur et al. 2010) to look for the signature of the modes, without success.

We also computed the predicted amplitude of the modes according to the seismic scaling relations taking $T_{\text{eff}} = 6000$ K and the Gaia luminosity of the star. We found a predicted amplitude of 5–6 ppm. In Fig. A3, we show that the amplitude spectrum between 500 and 200 μHz is completely flat, dominated by the noise with a mean value of 6.6 ppm which is higher than the expected amplitude of the modes. If the star was more evolved (late subgiant or early red giant), the modes would have been at lower frequency with higher amplitudes and we would have detected them. Thus we can only conclude that the star could either be on the main sequence or an early subgiant, which is consistent with our age determination. The graphs for our analysis are presented in Appendix A3.

3.2.5 TOI-1181b is a hot Jupiter around a subgiant

As explained above, in order to derive the planetary parameters and the orbital solution, we performed a joint fit with the TLMC package that combined all data sets from the spectroscopic instruments and from *TESS*. The fitted ratio of R_{planet}/R_* and inclination $i = 87.0^\circ \pm 1.3^\circ$ combined with the stellar radius R_* provides a planetary radius $R_{\text{planet}} = 1.30 \pm 0.08 R_J$. The planetary mass from the spectroscopic data and inclination i results in $M_{\text{planet}} = 1.18 \pm 0.14 M_J$. An orbital period $P = 2.103195^{+0.000012}_{-0.000011}$ was derived from the fit. All fitted parameters, for each instrument, are presented in Table 2. The folded *TESS* light curve is presented in Fig. 5 and RVs are presented in Fig. 6. Based on all our solutions, we are thus seeing a star which left the main sequence just recently and which is orbited by a hot Jupiter.

3.3 TOI-1516b: a hot Jupiter with a 2.05-d period

We used the *TESS* light curve and spectroscopic data from Tautenburg, Ondřejov, and McDonald observatories for a joint fit. In total we used 81 spectra from all three observatories.

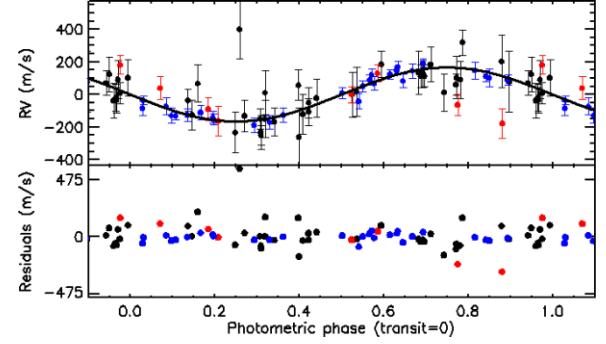


Figure 6. Upper panel: Phase-folded radial velocity measurements of TOI-1181. The black dots are the TCES measurements, the red dots the Ondřejov Echelle Spectrograph (OES) measurements, while the blue ones represent RVs obtained by the Tull spectrograph. The black solid line shows the circular orbit fit. Lower panel: Residuals of the radial velocity fit (in m s^{-1}).

3.3.1 The host Star TOI-1516

We stacked nine spectra from Ondřejov in order to determine the stellar parameters of the host star. The derivation of stellar parameters with ISPEC revealed that the host star has an effective temperature $T_{\text{eff}} = 6520 \pm 90$ K, a metallicity $[\text{Fe}/\text{H}] = -0.05 \pm 0.1$, surface gravity, $\log g = 4.25 \pm 0.15 \text{ cm s}^{-2}$, and $v \sin i = 11.8 \pm 1.5 \text{ km s}^{-1}$. All parameters are presented in the corresponding central column of Table 2. The spectral type and luminosity class found from our spectra as described in 3.2.1 is F8V.

A periodogram analysis was performed on the *TESS* data for TOI-1516. The dominant peak was found to be at 0.470 c/d (2.13 d), complemented with a group of other peaks in the low-frequency regime (the middle panel of Fig. 4). We detected a peak at the expected rotational frequency calculated from $v \sin i$ and stellar radius (the grey dash-dotted line in Fig. 4) also in one of the subsets. However, the detection is inconclusive.

We used ARIADNE to fit the SED and to determine the stellar parameters and age of the system. We used the derived stellar values from Table 2 as priors for ARIADNE. The SED obtained from the available photometric data as described in the Section 3.2.1 is depicted in the central panel of Fig. 3. The stellar mass from the isochrones was determined as $M_* = 1.085^{+0.061}_{-0.066} M_\odot$ and the stellar radius $R_* = 1.245^{+0.031}_{-0.032} R_\odot$. The age of the host star was determined as $4.82^{+2.44}_{-1.29}$ Gyr. For the derivation of the above parameters, the Gaia EDR3 parallax $\varpi = 0.0540 \pm 0.0098$ mas was used.

3.3.2 Planet TOI-1516b is another ordinary hot Jupiter

We performed a joint fit with TLMC. We performed the first fit with eccentricity as a free parameter and based on the result being consistent with a circular orbit, we fixed the eccentricity e at 0. Other parameters were left free. The resulting folded light curve from *TESS* is presented in Fig. 7 and the RVs are shown in Fig. 8. The values of the fit confirm that TOI-1516 b is a hot Jupiter with a 2.06-d orbital period. The values for the mass and the radius are $M = 3.16 \pm 0.12 M_J$ and $R = 1.36 \pm 0.03 R_J$, respectively. The derived parameters for the system imply an ordinary hot Jupiter around an F-type main sequence star.

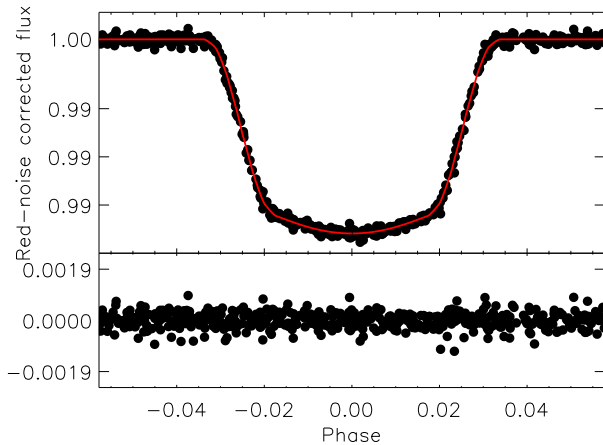


Figure 7. Same as Fig. 5 for TOI-1516.

3.4 The young system TOI-2046

We used data from *TESS* and from the Tautenburg, Ondřejov, and McDonald observatories. In total, we used 51 spectra from all three observatories. The corresponding RVs are listed in Table A3.

3.4.1 The host star TOI-2046

We stacked seven spectra from Ondřejov in order to determine the stellar parameters of the host star. Our analysis with ISPEC resulted in the following parameters for the host star: $T_{\text{eff}} = 6250 \pm 0.140$ K, metallicity $[\text{Fe}/\text{H}] = -0.06 \pm 0.15$, surface gravity, $\log g = 4.3 \pm 0.15$ cm s $^{-2}$, and $v \sin i = 9.8 \pm 1.6$ km s $^{-1}$. All relevant physical parameters are presented in the right column of Table 2. The spectral type and luminosity class determined as described in Section 3.2.1 is F8V.

3.4.2 Stellar activity

The dominant peak in the frequency spectrum of the full data set of TOI-2046 with the transit signature removed is at 0.252 c/d (period of 3.97 d) with a $\text{SNR} > 12$. To test the stability and reliability of the detected peak, we split the full data set into two subsets divided by the large gap between observations in sectors 18 + 19 (subset 1) and sectors 24 (subset 2) – see the bottom right-hand panel of Fig. 1. The peak is present in both subsets and has similar amplitude (blue and red lines in the bottom right-hand panel of Fig. 4).

The flux variations with the 4-d period are clearly apparent from the inset of the bottom panel of Fig. 4. The detection of the peak in the two subsets separated by more than 100 d shows that the frequency is stable over time. Thus, we assume that the variations are real (i.e. not instrumentals) and can be attributed to the stellar rotation with a period of 3.97(2) d.

The value of the detected rotational period significantly differs from the period calculated from $v \sin i$ and stellar radius ($P_{\text{rot}} \approx 6.2$ d). This may indicate that the rotational axis of the star and the orbital-plane axis of the planet are not aligned. The inclination of the rotational axis would be approximately 39° which is significantly different from the orbital inclination of the planet (83.6°).

3.4.3 Stellar age

ARIADNE yields an age of $0.45^{+0.43}_{-0.02}$ Gyr for TOI-2046, indicating that this is one of the few very young known planetary systems. We tried

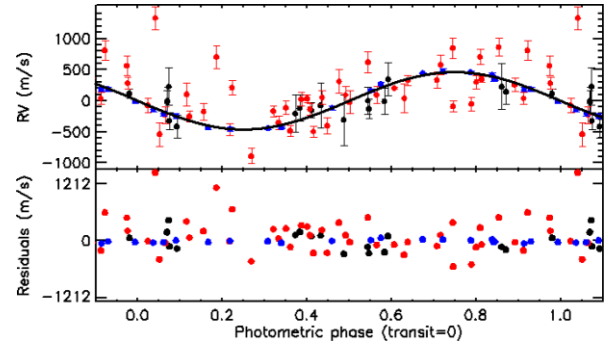


Figure 8. Same as Fig. 6 for TOI-1516.

to confirm the young age of the star using the Li line, which can be used as an indication of stellar youth. We measured the EWs of a Gaussian fit to the Li line at 6707 Å: $\text{EW} = 0.083 \pm 0.01$ Å. The EW and the derived stellar temperature from Table 2 were compared with available data from open clusters of various ages, shown in Fig. 9. A further discussion of the age of this particular system is provided in Section 4

3.4.4 A young hot Jupiter TOI-2046b

The folded *TESS* light curve is presented in Fig. 10 and the RVs in Fig. 11. The parameters of the planet from the joint fit with the TLCD package confirm that TOI-2046b is a hot Jupiter on an orbit with a 1.49-d period and a combination with stellar parameters allows for the determination of mass $M = 2.30 \pm 0.28$ M_J and radius $R = 1.44 \pm 0.11$ R_J .

4 NEW GAS PLANETS IN CONTEXT WITH OTHER GIANT PLANETS

In this section we will discuss the parameters of the newly discovered hot Jupiters in the context of similar systems.

4.1 Mass–radius diagram

The natural metrics for comparison of planets is the mass–radius diagram. We present the mass–radius diagram with the new *TESS* giant planets from this paper and plot them with all known planets which have parameters available in THE EXTRASOLAR PLANETS ENCYCLOPEDIA.⁶ The three hot Jupiters described in this paper exhibit rather larger radii, as can be seen in Fig. 12. We also show in the figure a set of recently discovered *TESS* hot Jupiters (Rodríguez et al. 2021) as a comparison with similar planets.

4.2 Incident flux from the host star and exo-atmospheres

We further investigated the incident flux from the host star at the planetary surface. For our three targets, we used Gaia DR2 and the luminosities determined with the *FLAMES* pipeline (Bailer-Jones et al. 2013). The resulting insolation are presented in Fig. 13, where the planetary equilibrium temperatures are also indicated. In the same figure, as a dashed line, we plot the empirical relationship for

⁶<http://exoplanet.eu/catalog>

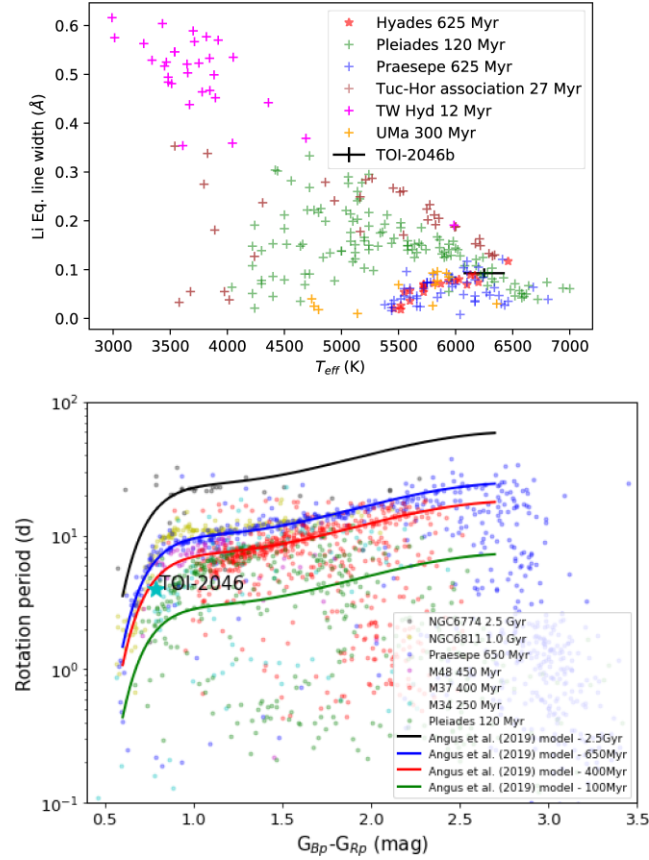


Figure 9. The top panel shows the equivalent widths (EWs) of the 6708 Å Li I line versus the effective temperatures for stars in selected young clusters and associations of different ages. The bottom panel presents the stellar rotational period versus their Gaia colour index for stars in several clusters, together with some models of cluster evolution represented with solid lines (Angus et al. 2019). In both panels, the data are from Soderblom et al. (1990, 1993a, b) and Mentuch et al. (2008), and the position of TOI-2046b is indicated.

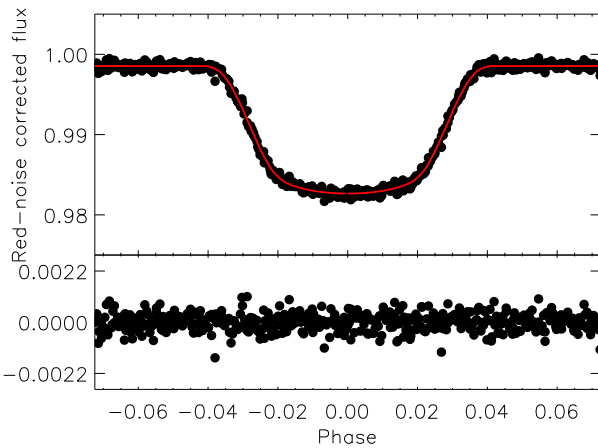


Figure 10. Same as Fig. 5 for TOI-2046.

one Jupiter-mass gas planets derived by Weiss et al. (2013, their equation 9):

$$\frac{R_p}{R_\oplus} = 2.45 \left(\frac{M_p}{M_\oplus} \right)^{-0.039} \left(\frac{F}{\text{erg s}^{-1} \text{cm}^{-2}} \right)^{0.094}, \quad (2)$$

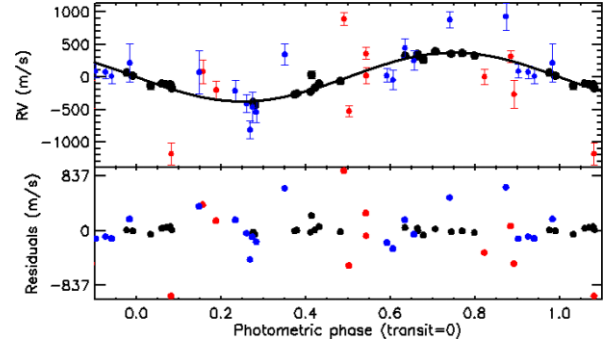


Figure 11. Same as Fig. 6 for TOI-2046.

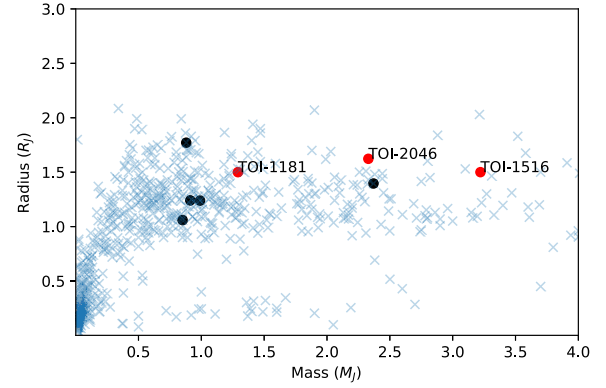


Figure 12. Mass–radius diagram of all known exoplanets with our three new systems represented by red dots. The black dots are some other recently discovered *TESS* gas giants (Rodríguez et al. 2021), shown for comparison.

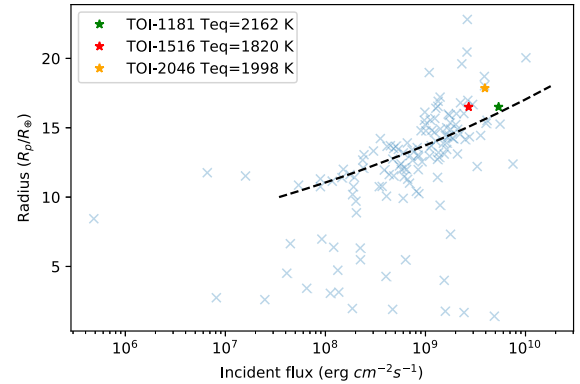


Figure 13. Radius versus incident flux for the three hot Jupiters from this paper including their equilibrium temperatures. Other known planets are represented by blue crosses. The dashed line represents the empirical relation from Weiss et al. (2013) for Jupiter-mass planets (equation 2).

where F is the incident flux and R_p and M_p are the planet’s radius and mass.

The three hot Jupiters reported in this paper receive higher incident flux from their host star compared to the majority of known planets. The highest insolation is consistent with the subgiant status of TOI-1181b, but TOI-2046b also undergoes high insolation and is most likely inflated. Therefore, these systems might in principle be reasonable candidates for further follow-up observations to detect their atmospheric signatures. For this reason, we calculated the expected atmospheric signal for performing transmission spectroscopy.

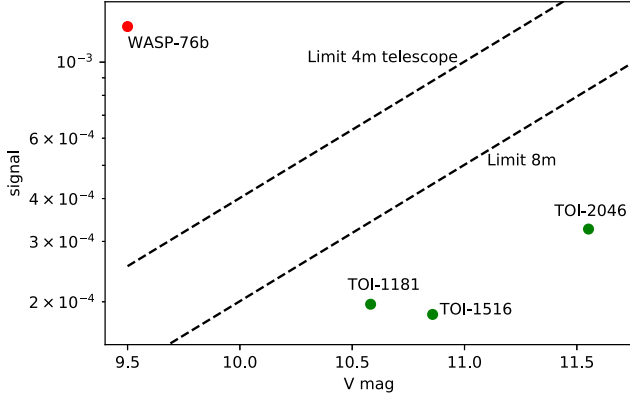


Figure 14. Expected signal of a planetary atmosphere, representative of the possible detection of the planet’s NaD lines by transmission spectroscopy. We also show the position of Wasp-76b, a reference system with a clear detection of Na, while the dashed lines show the detection limit for two classes of telescopes.

We followed the approach from Kabáth et al. (2019) and we first determined the expected signature of exoatmosphere $\Delta\delta$ roughly given by

$$\Delta\delta \approx \frac{2nHR_p}{R_s^2}, \quad (3)$$

where n is the number of atmospheric scale heights H . Here we assume $n = 6$ which is valid for high altitudes and typical for Na species abundant in gas giants. The expected signal for the three new hot Jupiters is presented in Fig. 14. We used as a reference a successful detection of the NaD features in the exoatmosphere of Wasp-76b and scaled down the detection limit at 3σ represented with a dashed line for a 4-m telescope and for an 8-m telescope. The three new planets have clearly an expected atmospheric signature too faint to be detected from the ground. However, the transmission signal $\Delta\delta = 326$ ppm from TOI-2046b should be clearly detectable by *JWST*, assuming the detection floor of 20 ppm for GJ1214b (Kreidberg et al. 2014; Greene et al. 2016) and taking into account the fact that our star is about 1.5 mag fainter in the K-band. Planets TOI-1181b and TOI-1516b would be definitively more challenging targets.

The high incident flux and relatively high atmospheric equilibrium temperatures make these targets interesting for detection of occultation of the planet by the star. Our team therefore analysed in detail the phased *TESS* light curves of these candidates with respect to the reflected light from the planet and new results will be presented in a separate paper (Csizmadia, in preparation) for TOI-1181b. However, it would be interesting to search for an occultation of TOI-2046b due to its rather high insolation and inflated atmosphere. The limiting factor for *TESS* is that TOI-2046 is one magnitude fainter than TOI-1181, leading to a much worse precision, and the analysis of the TOI-2046 *TESS* light curve is inconclusive.

4.3 A giant planet around a subgiant star

We know much less planets orbiting evolved stars than planets around main sequence stars. New planetary systems around evolved stars hosting a hot Jupiter were reported, e.g. with *Kepler* and *K2*, but also with *TES* (Döllinger et al. 2007; Van Eylen et al. 2016; Grunblatt et al. 2017). Planets around evolved stars usually show slightly larger eccentricities compared to planets around main sequence stars – the median for hot Jupiters main sequence stars is $0.056^{+0.022}_{-0.006}$, while

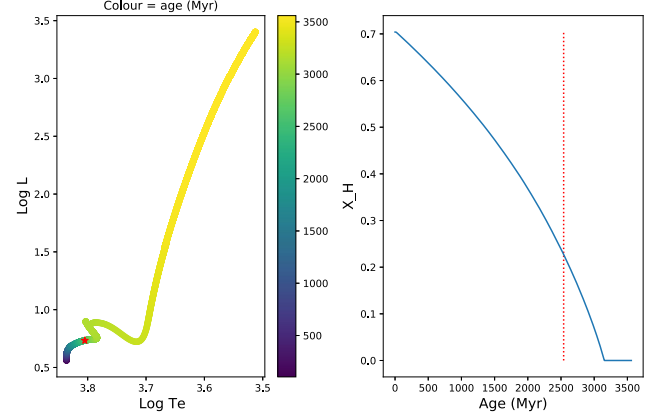


Figure 15. Left-hand panel: PARSEC evolutionary track in the Hertzsprung–Russell diagram of a $1.38 M_{\odot}$ star, corresponding to TOI-1181. The colours correspond to the age of the star (in Gyr), and the current position of TOI-1181 is indicated with the red dot. Right-hand panel: Fraction of remaining hydrogen in the core of the star, based on the PARSEC track, as a function of age, with the estimated age of TOI-1181 indicated with the vertical line.

for hot Jupiters around evolved stars it is $0.152^{+0.077}_{-0.042}$ (Grunblatt et al. 2018). However, in our case, we found the eccentricity of TOI-1181b to be consistent with zero. This system is also interesting due to its age of $2.59^{+0.43}_{-0.51}$ Gyr which is around the tipping point where the star leaves the main sequence and evolves towards the red giant branch, as can be seen in Fig. 15 which shows a PARSEC evolutionary track (Bressan et al. 2012). A star with a mass of $1.38 M_{\odot}$ has left the main sequence at the age of TOI-1181, even if its core still contains about 20 per cent of hydrogen.

The Gaia luminosity from DR2 data corresponds to $L = 4.45 \pm 0.08 L_{\odot}$. The derived $T_{\text{eff}} = 5990 \pm 95$ K corresponds to a F9 type star, but the radius $R = 1.9 R_{\odot}$ is too large for a main sequence star. The Gaia radius for the star TOI-1181 $R = 2.03 \pm 0.07 R_{\odot}$ is even larger than our values and it is also indicating an evolved star. The very early stage of the subgiant branch for this star is suggested also by our asteroseismologic analysis presented in Section 3.2.4 as we did not detect any pulsations typical for later stages of giant stars. The star rotates still relatively fast but when compared with the sample in e.g. do Nascimento et al. (2003), its rotation is consistent with a subgiant branch stars as can be seen in their Fig. 1. Therefore, tidal locking might play a role in a slower braking of the stellar rotation. From the presented analysis and from our spectral analysis described earlier, it can be concluded that we are seeing here an early subgiant star which entered its inflationary phase.

4.4 A very young hot-Jupiter system around TOI-2046

We now turn to the age of the TOI-2046 system and put it in context of other similar systems. Fig. 9 implies that the system TOI-2046 is a relatively young system, with an age between 27 Myr (Tucanae-Horologium association; Mentuch et al. 2008) and 625 Myr as a very conservative estimate (Praesepe or Hyades; Soderblom et al. 1993b, 1990). We also investigated the Gaia colour indices and rotational periods of selected young clusters and compared them to the TOI-2046 system’s parameters (see bottom of Fig. 9) as well as to evolutionary models of young clusters from Angus et al. (2019). The comparison of stellar rotational period constrains the age between 120 and 400 Myr. However, we remark that tidal spin-up would

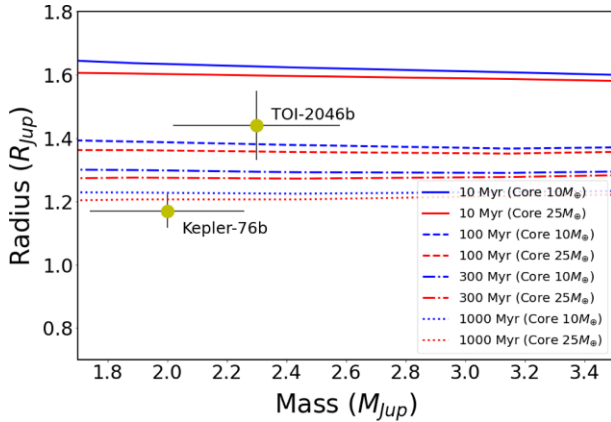


Figure 16. Mass–radius diagram with isochrones, according to thermal model by Fortney et al. (2007).

need to be taken into account if present (Tejada Arevalo, Winn & Anderson 2021).

We used the thermal evolution model (Fortney, Marley & Barnes 2007) to determine the core mass of this young system. As input parameters for the isochrones in the mass–radius graph, we use the systems parameters, the luminosity, and a distance from Gaia DR2 and EDR3 release, respectively. In Fig. 16, we show the isochrones in the mass radius diagram for different core sizes and we compare the planet TOI-2046b with Kepler-76b (Faigler et al. 2013), which has similar parameters but is older – around 1 Gyr of age. Fig. 16 would indicate an age below 100 Myr for our planet. However, it is more likely that the system is older and the planet is inflated as it undergoes high insolation. Indeed, the mechanism of inflation is not taken into account in the thermal model by Fortney et al. (2007) and the planet thereby appears younger in Fig. 16 than it is from gyrochronology (120–400 Myr) and from comparison of the lithium content with stars in open clusters (27–625 Myr).

To date, the youngest known hot Jupiter planet is HIP 67522 b orbiting the 17 ± 2 Myr old G1V star (Rizzuto et al. 2020). The second youngest gas giant orbits the 20 ± 6 Myr old 51 Eri star (Macintosh et al. 2015). Another candidate for a young exoplanetary system hosting gas giants is HR 8799, but the range of age estimates is large, going from 30 Myr to 1.1 Gyr (Song et al. 2001; Marois et al. 2008; Moya et al. 2010), with a most probable solution around 155 Myrs (Sudol & Haghighipour 2012). Recently, a few more young systems were presented in fig. 18 of Benatti et al. (2021), with ages in the range of 100–400 Myr. However, TOI-2046 is still only one of the handful fully characterized exoplanetary systems of such a very young age hosting a hot Jupiter.

Finally, we would like to stress that TOI-2046b is also a good candidate for the measurement of the Rossiter–McLaughlin effect. This has an expected amplitude of 80 m s^{-1} . The measurement of the spin axis alignment for this young system may reveal more details of its evolutionary stage.

5 CONCLUSIONS

In this paper we present the detection and characterization of three new hot Jupiters, TOI-1181b, TOI-1516b, and TOI-2046b, which were discovered by the *TESS* space mission. We confirmed the planetary candidates by a network of instruments installed on mid-aperture sized telescopes using the *KESPRINT* consortium observing time. Two of the newly detected systems, namely TOI-1181b and

TOI-1516b, are hot Jupiters with short orbital periods between 1.40 and 2.05 d, orbiting a G-type subgiant star and a main sequence F-type star, respectively. TOI-2046b, orbiting a main-sequence star, is a very young planetary system with an age between 30 and 625 Myr, making it one of the handful known systems so young. Young systems are extremely important for understanding the formation and evolution of hot Jupiters and thus further studies of this planetary system, such as an analysis of the orbital dynamics, more precise determination of its age, and perhaps also potential detection of an exo-atmosphere from space would be extremely important.

Finally, this paper clearly demonstrates that a network of telescopes with mid-sized apertures with suitable instrumentation can be used as a powerful tool for confirmation and characterization of hot Jupiter planets. Annually, about 90–135 nights of clear weather are available at Ondrejov Observatory (Kabáth et al. 2020). Observing runs aiming for characterization of giant planets are thus ideal targets for 2–4 m instruments, leaving valuable telescope time at large observatories for smaller planets.

ACKNOWLEDGEMENTS

This work is done under the framework of the KESPRINT collaboration (<http://www.kesprint.science>). KESPRINT is an international consortium devoted to the characterization and research of exoplanets discovered with space-based missions. This work is based on data sets obtained with the *Perek* 2-m telescope. PK, JS, MS, RK, and MB are acknowledging the support by Inter-transfer grant no LTT-20015. MK acknowledges the support from ESA-PRODEX PEA4000127913. PK and JS acknowledge a travel budget from ERASMUS + grant 2020-1-CZ01-KA203-078200. HB’s mobility was funded under: MŠMT – CZ.02.2.69/0.0/0.0/18_053/0016972 Podpora mezinárodní spolupráce v astronomii. PC acknowledges the generous support from Deutsche Forschungsgemeinschaft (DFG) of the grant CH 2636/1-1. PR acknowledges support from National Science Foundations (NSF) grant No. 1952545. This work was generously supported by the Thüringer Ministerium für Wirtschaft, Wissenschaft und Digitale Gesellschaft. We acknowledge the use of public TESS data from pipelines at the TESS Science Office and at the TESS Science Processing Operations Center. Resources supporting this work were provided by the NASA High-End Computing (HEC) Program through the NASA Advanced Supercomputing (NAS) Division at Ames Research Center for the production of the SPOC data products. JIV acknowledges support of CONICYT-PFCHA/Doctorado Nacional-21191829. This work is partly supported by JSPS KAKENHI Grant Number JP20K14518. JK gratefully acknowledge the support of the Swedish National Space Agency (SNSA; DNR 2020-00104). HD acknowledges support from the Spanish Research Agency of the Ministry of Science and Innovation (AEI-MICINN) under grant PID2019-107061GB-C66, DOI: 10.13039/501100011033. RL acknowledges financial support from the Spanish Ministerio de Ciencia e Innovación, through project PID2019-109522GB-C52, and the Centre of Excellence ‘Severo Ochoa’ award to the Instituto de Astrofísica de Andalucía (SEV-2017-0709). This work has made use of data from the European Space Agency (ESA) mission Gaia (<https://www.cosmos.esa.int/gaia>), processed by the Gaia Data Processing and Analysis Consortium (DPAC; <https://www.cosmos.esa.int/web/gaia/dpac/consortium>). Funding for the DPAC has been provided by national institutions, in particular the institutions participating in the Gaia Multilateral Agreement. This is University of Texas Center for Planetary Systems Habitability contribution #0054.

LGC acknowledges support from grant FPI-SO from the Spanish Ministry of Economy and Competitiveness (MINECO) (research project SEV-2015-0548-17-2 and predoctoral contract BES-2017-082610). SM acknowledges support by the Spanish Ministry of Science and Innovation with the Ramon y Cajal fellowship number RYC-2015-17697 and the grant number PID2019-107187GB-I00. RAG acknowledges the support from PLATO and GOLF CNES grants.

This paper includes data collected with the TESS mission, obtained from the MAST data archive at the Space Telescope Science Institute (STScI). Funding for the TESS mission is provided by the NASA Explorer Program. STScI is operated by the Association of Universities for Research in Astronomy, Inc., under NASA contract NAS 5-26555. Observations in the paper made use of the NN-EXPLORE Exoplanet and Stellar Speckle Imager (NESSI). NESSI was funded by the NASA Exoplanet Exploration Program and the NASA Ames Research Center. NESSI was built at the Ames Research Center by Steve B. Howell, Nic Scott, Elliott P. Horch, and Emmett Quigley. The authors are honored to be permitted to conduct observations on Iolkam Du’ag (Kitt Peak), a mountain within the Tohono O’odham Nation with particular significance to the Tohono O’odham people. This work is partly supported by JSPS KAKENHI Grant Number JP17H04574 and JP18H05439, JST PRESTO Grant Number JPMJPR1775, the Astrobiology Center of National Institutes of Natural Sciences (NINS; Grant Number AB031010). This article is based on observations made with the MuSCAT2 instrument, developed by ABC, at Telescopio Carlos Sánchez operated on the island of Tenerife by the IAC in the Spanish Observatorio del Teide.

Observations in the paper made use of the High-Resolution Imaging instrument ‘Alopeco. ‘Alopeco was funded by the NASA Exoplanet Exploration Program and built at the NASA Ames Research Center by Steve B. Howell, Nic Scott, Elliott P. Horch, and Emmett Quigley. ‘Alopeco was mounted on the Gemini North telescope of the international Gemini Observatory, a program of NSF’s NOIRLab, which is managed by the Association of Universities for Research in Astronomy (AURA) under a cooperative agreement with the National Science Foundation on behalf of the Gemini partnership: the National Science Foundation (United States), National Research Council (Canada), Agencia Nacional de Investigación y Desarrollo (Chile), Ministerio de Ciencia, Tecnología e Innovación (Argentina), Ministério da Ciência, Tecnologia, Inovações e Comunicações (Brazil), and Korea Astronomy and Space Science Institute (Republic of Korea).

This work was enabled by observations made from the Gemini North telescope, located within the Maunakea Science Reserve and adjacent to the summit of Maunakea. We are grateful for the privilege of observing the Universe from a place that is unique in both its astronomical quality and its cultural significance. We thank the anonymous referees for the useful suggestions to improve the paper.

DATA AVAILABILITY

The article presents results based on data sets from the *TESS* mission, which are available at Mikulski Archive. Furthermore, the radial velocity data values are provided in the article whereas the raw and calibrated data are available upon request to the observatory archives of Tautenburg and Ondřejov and from the authors with an affiliation at the University of Texas for Tull data.

REFERENCES

- Allard F., Homeier D., Freytag B., 2012, *Phil. Trans. R. Soc.*, 370, 2765
- Anderson D. R. et al., 2011, *ApJ*, 726, L19
- Angus R. et al., 2019, *AJ*, 158, 173
- Bailer-Jones C. A. L. et al., 2013, *A&A*, 559, A74
- Barragán O. et al., 2018, *MNRAS*, 475, 1765
- Barragán O., Gandolfi D., Antoniciello G., 2019, *MNRAS*, 482, 1017
- Batygin K., Bodenheimer P. H., Laughlin G. P., 2016, *ApJ*, 829, 114
- Benatti S. et al., 2021, *A&A*, 650, A66
- Blanco-Cuaresma S., 2019, *MNRAS*, 486, 2075
- Blanco-Cuaresma S., Soubiran C., Heiter U., Jofré P., 2014, *A&A*, 569, A111
- Bluhm P. et al., 2020, *A&A*, 639, A132
- Breger M. et al., 1993, *A&A*, 271, 482
- Bressan A., Marigo P., Girardi L., Salasnich B., Dal Cero C., Rubele S., Nanni A., 2012, *MNRAS*, 427, 127
- Brown T. M., 1991, *ApJ*, 371, 396
- Butler R. P., Marcy G. W., Williams E., McCarthy C., Dosanji P., Vogt S. S., 1996, *PASP*, 108, 500
- Carleo I. et al., 2020, *AJ*, 160, 114
- Carter J. A., Winn J. N., 2009, *ApJ*, 704, 51
- Castelli F., Kurucz R. L., 2006, *A&A*, 454, 333
- Cauley P. W., Wang J., Shkolnik E. L., Ilyin I., Strassmeier K. G., Redfield S., Jensen A. G., 2021, *AJ*, 161, 152
- Ciardi D. R., Beichman C. A., Horch E. P., Howell S. B., 2015, *ApJ*, 805, 16
- Csizmadia Sz., 2020, *MNRAS*, 496, 4442
- Csizmadia Sz., Smith A. M. S., Cabrera J., Klagyivik P., Chaushev A., Lam K. W. F., 2021, preprint ([arXiv:2108.11822](https://arxiv.org/abs/2108.11822))
- do Nascimento J. D. J., Canto Martins B. L., Melo C. H. F., Porto de Mello G., De Medeiros J. R., 2003, *A&A*, 405, 723
- Döllinger M. P., Hatzes A. P., Pasquini L., Guenther E. W., Hartmann M., Girardi L., Esposito M., 2007, *A&A*, 472, 649
- Döllinger M. P., Hatzes A. P., Pasquini L., Guenther E. W., Hartmann M., Girardi L., 2009, *A&A*, 499, 935
- Dotter A., 2016, *ApJS*, 222, 8
- Eastman J. D. et al., 2019, preprint ([arXiv:1907.09480](https://arxiv.org/abs/1907.09480))
- Eigmüller P. et al., 2017, *AJ*, 153, 130
- Endl M., Cochran W. D., 2016, *PASP*, 128, 094502
- Endl M., Kürster M., Els S., 2000, *A&A*, 362, 585
- Esposito M. et al., 2019, *A&A*, 623, A165
- Faigler S., Mazeh T., 2011, *MNRAS*, 415, 3921
- Faigler S., Tal-Or L., Mazeh T., Latham D. W., Buchhave L. A., 2013, *ApJ*, 771, 26
- Fortney J. J., Marley M. S., Barnes J. W., 2007, *ApJ*, 659, 1661
- Frasca A., Alcalá J. M., Covino E., Catalano S., Marilli E., Paladino R., 2003, *A&A*, 405, 149
- Fressin F. et al., 2013, *ApJ*, 766, 81
- Fridlund M. et al., 2020, *MNRAS*, 498, 4503
- Gaia Collaboration, 2016, *A&A*, 595, A1
- Gaia Collaboration, 2018, *A&A*, 616, A1
- Gandolfi D. et al., 2008, *ApJ*, 687, 1303
- Gandolfi D. et al., 2019, *ApJ*, 876, L24
- Gao P. et al., 2020, *Nature Astron.*, 4, 951
- García R. A. et al., 2011, *MNRAS*, 414, L6
- García R. A. et al., 2014, *A&A*, 568, A10
- Gray D. F., Brown K. I. T., 2006, *PASP*, 118, 399
- Greene T. P., Line M. R., Montero C., Fortney J. J., Lustig-Yaeger J., Luther K., 2016, *ApJ*, 817, 17
- Grunblatt S. K. et al., 2017, *AJ*, 154, 254
- Grunblatt S. K. et al., 2018, *ApJ*, 861, L5
- Grziwa S. et al., 2016, *AJ*, 152, 132
- Guenther E. W., Hartmann M., Esposito M., Hatzes A. P., Cusano F., Gandolfi D., 2009, *A&A*, 507, 1659
- Guerrero N. M. et al., 2021, *ApJS*, 254, 39
- Gustafsson B., Edvardsson B., Eriksson K., Jørgensen U. G., Nordlund Å., Plez B., 2008, *A&A*, 486, 951

- Hatzes A., Guenther E., Kürster M., 2003, in EGS - AGU - EUG Joint Assembly. European Geophysical Society, p. 6093
- Hauschildt P. H., Allard F., Baron E., 1999, *ApJ*, 512, 377
- Heller R., 2019, *A&A*, 628, A42
- Hjorth M. et al., 2019, *MNRAS*, 484, 3522
- Howell S. B., Everett M. E., Sherry W., Horch E., Ciardi D. R., 2011, *AJ*, 142, 19
- Howell S. B. et al., 2014, *PASP*, 126, 398
- Huang C. X. et al., 2020a, *Res. Notes Am. Astron. Soc.*, 4, 204
- Huang C. X. et al., 2020b, *Res. Notes Am. Astron. Soc.*, 4, 206
- Huang C. X. et al., 2020c, *ApJ*, 892, L7
- Husser T. O., Wende-von Berg S., Dreizler S., Homeier D., Reiners A., Barman T., Hauschildt P. H., 2013, *A&A*, 553, A6
- Jenkins J. M. et al., 2016, in Chiozzi G., Guzman J. C., eds, Proc. SPIE Conf. Ser. Vol. 9913, Software and Cyberinfrastructure for Astronomy IV. SPIE, Bellingham, p. 99133E
- Johnson M. C. et al., 2016, *AJ*, 151, 171
- Johnson M. C. et al., 2018, *MNRAS*, 481, 596
- Kabáth P., Žák J., Boffin H. M. J., Ivanov V. D., Jones D., Skarka M., 2019, *PASP*, 131, 085001
- Kabáth P. et al., 2020, *PASP*, 132, 035002
- Kjeldsen H., Bedding T. R., 1995, *A&A*, 293, 87
- Kreidberg L. et al., 2014, *Nature*, 505, 69
- Kurucz R., 1993, ATLAS9 Stellar Atmosphere Programs and 2 km/s grid. Kurucz CD-ROM No. 13. Smithsonian Astrophysical Observatory, Cambridge, p. 13
- Lenz P., Breger M., 2005, *Commun. Asteroseismology*, 146, 53
- Li J., Tenenbaum P., Twicken J. D., Burke C. J., Jenkins J. M., Quintana E. V., Rowe J. F., Seader S. E., 2019, *PASP*, 131, 024506
- Lightkurve Collaboration, 2018, Astrophysics Source Code Library, record ascl:1812.013
- Luque R. et al., 2021, *A&A*, 645, A41
- Macintosh B. et al., 2015, *Science*, 350, 64
- Marois C., Macintosh B., Barman T., Zuckerman B., Song I., Patience J., Lafrenière D., Doyon R., 2008, *Science*, 322, 1348
- Masuda K., Winn J. N., 2017, *AJ*, 153, 187
- Mathur S. et al., 2010, *A&A*, 511, A46
- Mayor M., Queloz D., 1995, *Nature*, 378, 355
- Mentuch E., Brandeker A., van Kerkwijk M. H., Jayawardhana R., Hauschildt P. H., 2008, *ApJ*, 689, 1127
- Morris R. L., Twicken J. D., Smith J. C., Clarke B. D., Jenkins J. M., Bryson S. T., Girouard F., Klaus T. C., 2020, in Jenkins J. M., ed., Kepler Science Document KSCI-19081-003. p. 6
- Moya A., Amado P. J., Barrado D., García Hernández A., Aberasturi M., Montesinos B., Aceituno F., 2010, *MNRAS*, 405, L81
- Narita N. et al., 2019, *J. Astron. Telescopes Instrum. Syst.*, 5, 015001
- Pollack J. B., Hubickyj O., Bodenheimer P., Lissauer J. J., Podolak M., Greenzweig Y., 1996, *Icarus*, 124, 62
- Ricker G. R. et al., 2014, Proc. SPIE, 9143, 914320
- Ricker G. R. et al., 2015, *J. Astron. Telescopes Instrum. Syst.*, 1, 014003
- Rizzuto A. C. et al., 2020, *AJ*, 160, 33
- Rodriguez J. E. et al., 2021, *AJ*, 161, 194
- Sabotta S., Kabáth P., Korth J., Guenther E. W., Dupkala D., Grziwa S., Klocova T., Skarka M., 2019, *MNRAS*, 489, 2069
- Scott N. J., 2019, in AAS/Division for Extreme Solar Systems Abstracts. American Astron. Soc., p. 330.15
- Shporer A., 2017, *PASP*, 129, 072001
- Smith A. M. S. et al., 2017, *MNRAS*, 464, 2708
- Smith A. M. S. et al., 2019, *AcA*, 69, 135
- Soderblom D. R., Oey M. S., Johnson D. R. H., Stone R. P. S., 1990, *AJ*, 99, 595
- Soderblom D. R., Pilachowski C. A., Fedele S. B., Jones B. F., 1993a, *AJ*, 105, 2299
- Soderblom D. R., Fedele S. B., Jones B. F., Stauffer J. R., Prosser C. F., 1993b, *AJ*, 106, 1080
- Song I., Caillault J. P., Barrado y Navascués D., Stauffer J. R., 2001, *ApJ*, 546, 352
- Sudol J. J., Haghighipour N., 2012, *ApJ*, 755, 38
- Šubjak J. et al., 2020, *AJ*, 159, 151
- Tejada Arevalo R. A., Winn J. N., Anderson K. R., 2021, *ApJ*, 919, 138
- Tull R. G., MacQueen P. J., Sneden C., Lambert D. L., 1995, *PASP*, 107, 251
- Twicken J. D., Clarke B. D., Bryson S. T., Tenenbaum P., Wu H., Jenkins J. M., Girouard F., Klaus T. C., 2010, in Radziwill N. M., Bridger A., eds, Proc. SPIE Conf. Ser. Vol. 7740, Software and Cyberinfrastructure for Astronomy. SPIE, Bellingham, p. 774023
- Twicken J. D. et al., 2018, *PASP*, 130, 064502
- Valdes F., Gupta R., Rose J. A., Singh H. P., Bell D. J., 2004, *ApJS*, 152, 251
- van Dokkum P. G., 2001, *PASP*, 113, 1420
- Van Eylen V. et al., 2016, *AJ*, 152, 143
- Van Eylen V. et al., 2021, *MNRAS*, 507, 2154
- Vines J., Jenkins J. E. A. I. P., 2022, *MNRAS*, 513, 2719
- Wang J., Fischer D. A., Horch E. P., Huang X., 2015, *ApJ*, 799, 229
- Weiss L. M. et al., 2013, *ApJ*, 768, 14
- Weiss L. M. et al., 2017, *AJ*, 153, 265
- Winn J. N., 2010, preprint ([arXiv:1001.2010](https://arxiv.org/abs/1001.2010))
- Wong I. et al., 2020, *AJ*, 159, 104
- Wright J. T., Upadhyay S., Marcy G. W., Fischer D. A., Ford E. B., Johnson J. A., 2009, *ApJ*, 693, 1084
- Wytenbach A., Ehrenreich D., Lovis C., Udry S., Pepe F., 2015, *A&A*, 577, A62
- Yan F. et al., 2021, *A&A*, 645, A22
- Zechmeister M., Köhler J., Chamarthi S., 2021, Astrophysics Source Code Library, record ascl:2108.006
- Žák J., Kabáth P., Boffin H. M. J., Ivanov V. D., Skarka M., 2019, *AJ*, 158, 120

SUPPORTING INFORMATION

Supplementary data are available at [MNRAS](https://www.mnras.org) online.

mnras.hotjupitersaccept-appendix.pdf

Please note: Oxford University Press is not responsible for the content or functionality of any supporting materials supplied by the authors. Any queries (other than missing material) should be directed to the corresponding author for the article.

APPENDIX A: ADDITIONAL TABLES AND FIGURES

Table A1. Parameters determined from the *MUSCAT2* light curve for TOI-1181.

Epoch	2458 766.43048	± 0.00054
Period	2.10319	± 0.00001 d
Stellar density	0.32550	± 0.00787 g cm ⁻³
Impact parameter	b < 0.28759	(99 per cent posterior upper limit)
Radius ratio	0.08683	± 0.00132

Table A2. Radial velocities of TOI-1181.

Date (BJD)	RV (m s ⁻¹)	σ_{RV} (m s ⁻¹)	Instrument
2458891.624504	119.2	137.2	TCES
2458891.646611	135.3	148.6	TCES
2458892.516390	244.2	106.3	TCES
2458892.538323	82.2	107.6	TCES
2458892.560290	210.4	118.0	TCES
2458913.581137	99.8	84.3	TCES
2458913.602628	127.5	65.5	TCES
2458916.594736	176.2	94.2	TCES
2458916.616264	-1.7	122.9	TCES
2458918.510222	-113.1	104.0	TCES
2458918.532270	130.4	136.5	TCES
2458923.503219	252.3	130.6	TCES
2458923.524388	246.5	83.3	TCES
2459000.453694	-13.5	96.6	TCES
2459001.510255	222.5	130.5	TCES
2459003.484689	303.2	106.1	TCES
2459006.530164	186.2	114.4	TCES
2459027.512966	83.1	68.2	TCES
2459066.549074	232.7	68.3	TCES
2459067.494285	-7.4	91.5	TCES
2459070.540453	304.1	80.3	TCES
2459094.407467	188.7	76.3	TCES
2459094.516228	221.0	113.7	TCES
2459095.456436	96.7	117.3	TCES
2459097.519515	68.9	95.2	TCES
2459098.518832	196.8	187.3	TCES
2459099.381413	-31.6	61.8	TCES
2459100.389551	438.4	77.1	TCES
2459100.585164	322.4	160.9	TCES
2459101.555221	-49.1	85.7	TCES
2459177.393867	-142.2	180.3	TCES
2459177.441483	13.1	82.7	TCES
2459179.306668	-130.3	59.4	TCES
2459179.327816	-30.9	114.0	TCES
2459180.278832	180.0	63.5	TCES
2459180.300000	208.8	114.9	TCES
2459181.281956	-113.7	122.3	TCES
2459181.303683	519.4	179.6	TCES
2459209.548487	231.2	71.8	TCES
2459209.663867	130.9	113.6	TCES
2459214.340952	82.9	79.5	TCES
2459067.574725	-89.0	72.0	OES
2459070.521985	131.0	54.0	OES
2459071.541575	38.0	70.0	OES
2459074.598145	0.0	50.0	OES
2459075.549465	182.0	57.0	OES
2459086.554015	-163.0	91.0	OES
2459100.588335	-177.0	91.0	OES
2459104.572505	-64.0	66.0	OES
2458951.925755	-136.7	32.9	Tull
2458957.885446	-21.7	27.8	Tull
2458994.903263	163.2	25.0	Tull
2459054.772528	-114.8	46.2	Tull
2459072.686735	138.7	29.8	Tull
2459073.722383	-117.1	21.6	Tull
2459090.733304	-124.8	38.8	Tull
2459091.680828	98.1	42.1	Tull
2459104.729921	115.1	55.3	Tull

Table A3. Radial velocities of TOI-1516.

Date (BJD)	RV (m s ⁻¹)	σ_{RV} (m s ⁻¹)	Instrument
2459209.57482	-177	302	TCES
2459209.61444	-821	179	TCES
2459214.38049	-556	127	TCES
2459094.43088	-408	214	TCES
2459095.50450	-56	268	TCES
2459097.54374	-417	209	TCES
2459098.54208	-422	182	TCES
2459099.40184	-714	408	TCES
2459099.51834	-405	221	TCES
2459100.41467	-291	81	TCES
2459100.60848	-730	137	TCES
2459101.57987	-534	152	TCES
2459177.41747	-483	363	TCES
2459179.35048	-611	300	TCES
2459179.37221	-524	213	TCES
2459180.35372	-178	366	TCES
2459180.37488	-264	190	TCES
2459209.57482	-177	302	TCES
2459209.61444	-821	179	TCES
2459214.38049	-556	127	TCES
2458863.25393	-474	233	OES
2458864.25126	-409	180	OES
2458865.26129	-310	20	OES
2458872.34369	-1054	191	OES
2458892.27580	-604	90	OES
2458892.36445	-568	110	OES
2458892.40691	193	123	OES
2458892.63805	298	152	OES
2458898.36529	-179	130	OES
2458901.27357	-764	92	OES
2458924.32249	-867	105	OES
2458924.55897	-915	128	OES
2458925.31019	-165	43	OES
2458926.51850	-478	60	OES
2458928.30224	-1404	124	OES
2458928.47061	-626	108	OES
2458931.27899	62	155	OES
2458931.56240	347	146	OES
2458932.30872	-973	96	OES
2458932.60401	-1000	87	OES
2458936.29387	-690	138	OES
2458936.63373	-679	88	OES
2458937.28739	-184	81	OES
2458937.62028	-213	104	OES
2458942.60106	-302	115	OES
2458946.38789	-745	137	OES
2458946.63689	191	183	OES
2458956.31205	-258	109	OES
2458956.35458	-475	95	OES
2458956.58365	-588	116	OES
2458956.61892	817	183	OES
2458957.32975	-489	113	OES
2458957.37191	-649	97	OES
2458959.56920	-201	190	OES
2458960.59308	47	154	OES
2458963.55698	-1007	90	OES
2458963.59917	-461	111	OES
2458976.57060	331	163	OES
2458990.55013	104	167	OES

Table A3 – *continued*

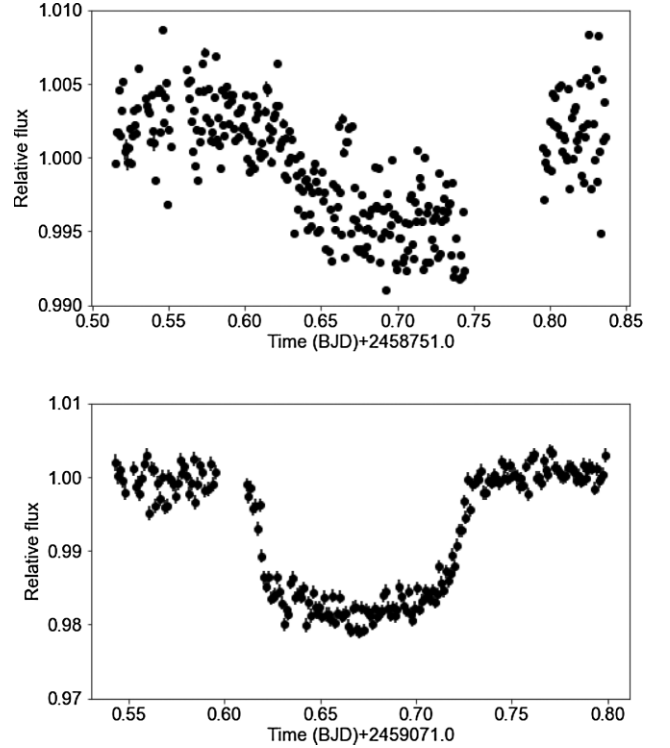
Date (BJD)	RV (m s ⁻¹)	σ_{RV} (m s ⁻¹)	Instrument
2458992.51773	-536	187	OES
2459101.61717	-419	141	OES
2459105.57857	-419	139	OES
2459106.57426	-229	95	OES
2458824.63161	-48227	35	Tull
2458824.77300	-48406	34	Tull
2459054.89122	-48166	29	Tull
2459072.85339	-48318	28	Tull
2459073.85204	-48793	35	Tull
2459090.80845	-49031	24	Tull
2459091.79470	-48130	23	Tull
2459104.75247	-48831	42	Tull
2459114.70318	-48407	31	Tull
2459115.79221	-48704	31	Tull
2459116.89061	-48600	30	Tull
2459133.80040	-49039	36	Tull
2459134.83585	-48109	45	Tull
2459144.76502	-48426	24	Tull
2459145.76340	-48731	29	Tull
2459171.74582	-48147	11	Tull
2459191.61890	-49023	19	Tull
2459192.65273	-48237	33	Tull
2459203.59849	-49018	28	Tull

Table A4. Radial velocities of TOI-2046.

Date (BJD)	RV (m s ⁻¹)	σ_{RV} (m s ⁻¹)	Instrument
2459099.93401	-237	10	Tull
2459099.94896	-179	22	Tull
2459099.96417	-110	23	Tull
2459100.90511	-115	26	Tull
2459100.92022	-125	21	Tull
2459100.93531	-131	40	Tull
2459114.85045	-280	15	Tull
2459115.83681	-145	57	Tull
2459116.94014	355	41	Tull
2459133.87820	-186	37	Tull
2459134.81185	377	17	Tull
2459143.73240	307	16	Tull
2459144.64706	-405	33	Tull
2459145.69545	55	24	Tull
2459170.70165	252	25	Tull
2459171.60259	-442	31	Tull
2459171.90490	-75	21	Tull
2459191.64141	346	35	Tull
2459192.71142	-264	30	Tull
2459202.61011	7	30	Tull
2459203.57473	314	18	Tull
2459203.82064	313	15	Tull
2459227.69379	346	21	Tull
2459240.67291	23	60	Tull
2459120.40138	-656	171	OES
2459160.43763	528	119	OES
2459175.51402	258	213	OES
2459184.48565	841	94	OES
2459188.46491	547	129	OES

Table A4 – *continued*

Date (BJD)	RV (m s ⁻¹)	σ_{RV} (m s ⁻¹)	Instrument
2459242.28485	1418	102	OES
2459246.27680	607	186	OES
2459266.25817	0	85	OES
2459269.31186	887	92	OES
2459270.27897	326	132	OES
2459246.26373	-9419	335	TCES
2459266.45564	-9047	142	TCES
2459270.52201	-9147	162	TCES
2459271.30546	-8563	206	TCES
2459298.29829	-9403	102	TCES
2459299.42600	-9237	151	TCES
2459299.55290	-8613	119	TCES
2459300.29025	-9705	167	TCES
2459303.32457	-9905	138	TCES
2459303.34573	-9958	232	TCES
2459304.32230	-9414	97	TCES
2459304.34403	-9478	121	TCES
2459305.31905	-9470	103	TCES
2459305.34021	-9538	153	TCES
2459309.32588	-10303	136	TCES
2459309.34761	-10030	163	TCES
2459310.39691	-9277	291	TCES

**Figure A1.** Light curves of TOI-1181 (left) and TOI-1516 (right) from the CRAO Observatory.

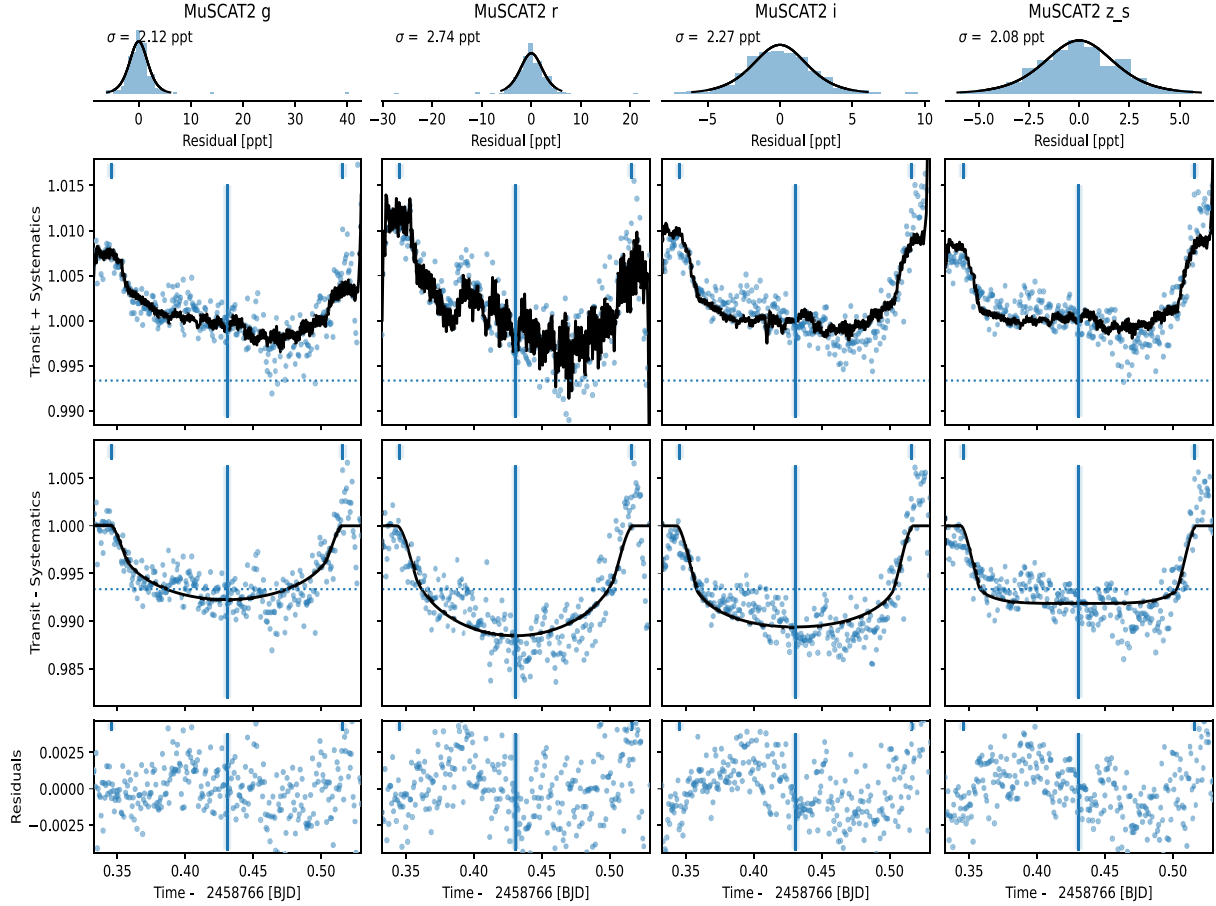


Figure A2. Light curves of the transit of TOI-1181b in different filters obtained with MUSCAT2.

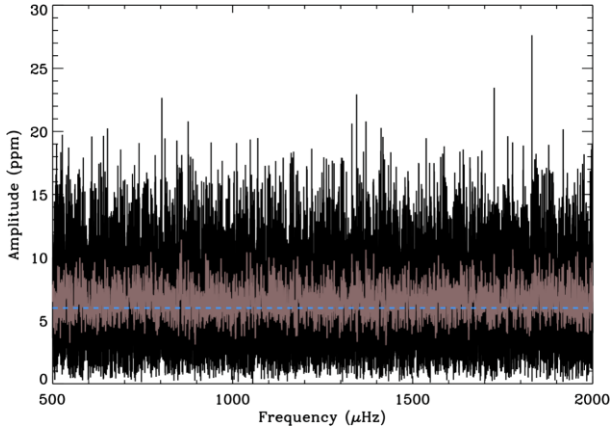


Figure A3. Amplitude spectrum as a function of the frequency (in black) where we superimposed a smoothed curve with an 11-point boxcar (in grey). The dash blue line corresponds to the expected amplitude of the modes of 6 ppm.

¹Astronomical Institute of the Czech Academy of Sciences, Fričova 298, 25165 Ondřejov, Czech Republic

²Thüringer Landessternwarte Tautenburg, Sternwarte 5, D-07778 Tautenburg, Germany

³McDonald Observatory, The University of Texas at Austin, Austin, TX 78712, USA

⁴Astronomical Institute of Charles University, V Holešovičkách 2, 180 00 Prague, Czech Republic

⁵Center for Planetary Systems Habitability and McDonald Observatory, The University of Texas, Austin, TX 78712, USA

⁶Dipartimento di Fisica, Università Degli Studi di Torino Via Pietro Giuria, 1, I-10125 Torino, Italy

⁷Center for Planetary Systems Habitability and Department of Astronomy, The University of Texas, Austin, TX 78712, USA

⁸Department of Extrasolar Planets and Atmospheres, German Aerospace Center, Rutherfordstrasse 2., D-12489 Berlin, Germany

⁹European Southern Observatory, Karl-Schwarzschild-Str. 2., D-85748 Garching bei Muenchen, Germany

¹⁰Departamento de Astronomía, Universidad de Chile, Casilla 36-D, Santiago, Chile

¹¹Department of Astronomy, University of Tokyo, 7-3-1 Hongo, Bunkyo-ku, 113-0033 Tokyo, Japan

¹²Laboratoire AIM, CEA/DSM - CNRS - Université Paris Diderot - IRFU/SAp, F-91191 Gif-sur-Yvette Cedex, France

¹³Instituto de Astrofísica de Canarias (IAC), E-38205 La Laguna, Tenerife, Spain

¹⁴Departamento de Astrofísica, Universidad de La Laguna (ULL), E-38206 La Laguna, Tenerife, Spain

¹⁵Department of Theoretical Physics and Astrophysics, Faculty of Science, Masaryk University, Kotlářská 267/2, 611 37 Brno, Czech Republic

¹⁶SETI Institute, 189 Bernardo Ave, Suite 200 Mountain View, CA 94043, USA

¹⁷NASA Goddard Space Flight Center, Greenbelt, MD 20771, USA

¹⁸Mullard Space Science Laboratory, University College London, Holmbury St Mary, Dorking, Surrey RH5 6NT, UK

¹⁹*Department of Physics and Kavli Institute for Astrophysics and Space Research, Massachusetts Institute of Technology, Cambridge, MA 02139, USA*

²⁰*Chalmers University of Technology, Department of Space, Earth and Environment, Onsala Space Observatory, SE-439 92 Onsala, Sweden*

²¹*Leiden Observatory, University of Leiden, PO Box 9513, 2300 RA, Leiden, The Netherlands*

²²*Komaba Institute for Science, The University of Tokyo, 3-8-1 Komaba, Meguro, 153-8902 Tokyo, Japan*

²³*Kavli Institute for Astrophysics and Space Research, Massachusetts Institute of Technology, Cambridge, MA 02139, USA*

²⁴*NASA Ames Research Center, Moffett Field, CA 94035, USA*

²⁵*Department of Space, Earth and Environment, Astronomy and Plasma Physics, Chalmers University of Technology, 412 96 Gothenburg, Sweden*

²⁶*Instituto de Astrofísica de Andalucía (IAA-CSIC), Glorieta de la Astronomía s/n, E-18008 Granada, Spain*

²⁷*Google, Cambridge, MA 02142, USA*

²⁸*Japan Science and Technology Agency, PRESTO, 3-8-1 Komaba, Meguro, 153-8902 Tokyo, Japan*

²⁹*Astrobiology Center, 2-21-1 Osawa, Mitaka, 181-8588 Tokyo, Japan*

³⁰*Department of Physical Sciences, Kutztown University, Kutztown, PA 19530, USA*

³¹*Astronomy Department and Van Vleck Observatory, Wesleyan University, Middletown, CT 06459, USA*

³²*Department of Earth, Atmospheric and Planetary Sciences, Massachusetts Institute of Technology, Cambridge, MA 02139, USA*

³³*Department of Aeronautics and Astronautics, Massachusetts Institute of Technology, 77 Massachusetts Avenue, Cambridge, MA 02139, USA*

³⁴*Department of Multi-Disciplinary Sciences, Graduate School of Arts and Sciences, The University of Tokyo, 3-8-1 Komaba, Meguro, 153-8902 Tokyo, Japan*

³⁵*Department of Astrophysical Sciences, Peyton Hall, 4 Ivy Lane, Princeton, NJ 08544, USA*

This paper has been typeset from a \LaTeX file prepared by the author.